Astronomy & Astrophysics manuscript no. output
April 29, 2025

Role of diffusive and non-diffusive grain-surface processes in cold cores: Insights from the PEGASIS three-phase astrochemical model

S. Maitrey[1,2], Liton Majumdar[1,2], Varun Manilal[1,2], Baibhav Srivastava[1,2], Prathap Rayalacheruvu[1,2], Karen Willacy[3], and Eric Herbst[4]

[1] Exoplanets and Planetary Formation Group, School of Earth and Planetary Sciences, National Institute of Science Education and Research, Jatni 752050, Odisha, India
e-mail: `liton@niser.ac.in; dr.liton.majumdar@gmail.com`
[2] Homi Bhabha National Institute, Training School Complex, Anushaktinagar, Mumbai 400094, India
[3] Jet Propulsion Laboratory, California Institute of Technology, 4800 Oak Grove Drive, Pasadena, CA 91109, USA
[4] Department of Chemistry, University of Virginia, Charlottesville, VA 22904, USA

April 29, 2025

ABSTRACT

Context. Cold dense cores are unique among the structures found in the interstellar medium, as they harbor a rich chemical inventory, including complex organic molecules (COMs), which will be inherited by future evolutionary stages, such as protostellar envelopes and protoplanetary disks. These molecules exist both in the gas phase and as ices accreted onto grain surfaces.
Aims. To model these environments, we present Pegasis, a new, fast, and extensible three-phase astrochemical code to explore the chemistry of cold cores, with an emphasis on the role of diffusive and non-diffusive chemistry in shaping their gas and grain chemical compositions.
Methods. We incorporate the latest developments in interstellar chemistry modeling by utilizing the 2024 KIDA chemical network and comparing our results with current state-of-the-art astrochemical models. Using a traditional rate-equation-based approach, we implement both diffusive and non-diffusive chemistry, coupled with either an inert or chemically active ice mantle.
Results. We identify crucial reactions that enhance the production of COMs through non-diffusive mechanisms on the grain-surface as well as the mechanisms through which they can build up in gas-phase. Across all models with non-diffusive chemistry, we observe a definite enhancement in the concentration of COMs on both grain-surface as well in the grain-mantle. Finally, our model broadly reproduces the observed abundances of multiple gas-phase species in a cold dense core TMC-1 (CP) and provides insights into its chemical age.
Conclusions. Our work demonstrates the capabilities of Pegasis in exploring a wide range of grain-surface chemical processes and modeling approaches for three-phase chemistry in the interstellar medium, providing robust explanations for observed abundances in cold cores, such as TMC-1 (CP). In particular, it highlights the role of non-diffusive chemistry in the production of gas-phase COMs on grain surfaces, which are subsequently chemically desorbed, especially when the precursors involved in their formation on the surfaces are heavier than atomic hydrogen.

Key words. astrochemistry / ISM: abundances / ISM: molecules / ISM: individual objects: TMC-1 (CP)

1. Introduction

The accretion of gas-phase interstellar molecules on the cold dust grains plays a fundamental role in enriching the chemistry of molecular clouds. These grains facilitate several processes, both physical and chemical, to proceed on their surface which in turn leads to the formation of species that cannot be solely formed in the gas phase (see Tielens & Hagen 1982; Herbst & van Dishoeck 2009, and references therein). For instance, Gould & Salpeter (1963) established that dust grains must act as catalysts to account for the presence of molecular hydrogen observed in the interstellar medium. The surface chemistry thus becomes the bridge which dictates the compositions of both the bulk ice that will exist on grains as well as the compositions of gas phase through desorption. Astrochemical models which can simulate these processes in the interstellar medium (and in various more evolved proto-stellar or protoplanetary environments) have existed ever since the use of radio observatories became prominent in detecting interstellar molecules (Agúndez & Wakelam 2013). As the list of observed molecules keeps growing (see the Cologne Database for Molecular Spectroscopy[1] and McGuire 2022, for the most recent compilation) with more advanced observational capabilities, it has became imperative for the models to keep evolving. A good astrochemical model must be able to couple gas-phase chemistry with ice chemistry while being versatile enough to be used in a variety of physical environments.

For cold cores, pioneering work by Bates & Spitzer (1951); Watson (1973, 1974, 1976) and Herbst & Klemperer (1973) established the key chemical processes and pathways that paved the way to construct chemical networks. In conjunction with experimental work, sets of reactions involving detected molecules that can occur in the interstellar medium are identified and compiled to be simulated by a numerical scheme. Currently, the UMIST Database for Astrochemistry (Millar et al. 1991,

---

[1] https://cdms.astro.uni-koeln.de/classic/molecules

1997; Le Teuff et al. 2000; Woodall et al. 2007; McElroy et al. 2013; Millar et al. 2024) and KInetic Database for Astrochemistry (KIDA) (Wakelam et al. 2012, 2015, 2024) represent the most recent and well-maintained publicly available networks. The chemical networks typically encapsulate information about which chemical reactions and processes can proceed under specific physical conditions. These networks then can be fed in and used by several astrochemical codes for modeling. A few examples among many published astrochemical codes include the Willacy Model (Willacy & Millar 1998); Alchemic (Semenov et al. 2010); Magickal (Garrod & Pauly 2011); GRAINOBLE (Taquet et al. 2012); MONACO (Vasyunin & Herbst 2013); astrochem[2] (Maret et al. 2013); the Rokko code (Furuya et al. 2015); the CMMC code (Das et al. 2015); Nautilus[3] (Ruaud et al. 2016); UCLCHEM[4] (Holdship et al. 2017); CHEMPL[5] (Du 2021); the Acharyya Model (Acharyya et al. 2020); and Sipilä's Model (Sipilä et al. 2022). Several of these codes are now publicly available for broader use within the astrochemistry community as well. The approaches used by these codes to simulate chemical networks vary, but the rate equation method, which involves solving a system of coupled differential equations, has proven to be straightforward to implement and faster to converge (see Cuppen et al. 2013, for an overview on this and other techniques).

Increasingly, theoretical and laboratory studies have highlighted the importance of physico-chemical processes such as photodissociation by UV radiation and cosmic rays, as well as diffusive chemistry, which extends beyond the gas phase to the grain surface and the bulk mantle (Andersson & van Dishoeck 2008; Öberg et al. 2009). This makes the inclusion of an active non-inert mantle crucial to evaluate the extent to which it can influence the wider gas phase chemistry. Several authors have attempted to implement this by considering each accreted ice layer distinctly (Taquet et al. 2012) or by considering multiple layer grouped as phases of the mantle (Furuya et al. 2017) as well as extending the three-phase model of Hasegawa & Herbst (1993b) to explore effects of bulk ice chemistry (Ruaud et al. 2016; Kalvāns & Shmeld 2010; Garrod 2013).

Inclusion of ice chemistry opens up the possibility of progressive entrapment of molecules onto the grains, as the gas phase reservoir depletes which reduces both the rates of accretion and desorption. Herbst et al. (2005) discusses the importance of non-thermal desorption pathways, especially, for much later ages in the total lifetime of cold cores. Works like Garrod et al. (2006) have discussed the role of desorption pathways in reproducing abundances at much later times. Essentially, consideration of a more detailed framework of ice chemistry and how it interacts with the gas phase have suggested a late convergence with the observations to an increasing extent (see Wakelam et al. 2021, for the most recent development). Thus, the estimation of chemical ages of these sources is still uncertain.

The inner regions of dense clouds are often well-shielded, allowing the bulk mantle to persist for extended periods. However, the very low temperatures in these regions ($\sim$ 10 K) render most heavier species immobile, making diffusion-driven production of complex organic molecules (COMs) unfeasible. This contrasts with the detection of molecules such as methyl formate ($HCOOCH_3$) and dimethyl ether (CH_3OCH_3) in colder regions (Cernicharo et al. 2012; Bacmann et al. 2012). Consequently, alternative pathways have been proposed to form these COMs on grain surfaces without relying on diffusive chemistry (Ruaud et al. 2015; Chang & Herbst 2016; Bergner et al. 2017a,b; Shingledecker et al. 2018; Jin & Garrod 2020), with subsequent non-thermal desorption mechanisms playing a crucial role. Notably, Balucani et al. (2015) also suggested the possibility of gas-phase formation of COMs. Jin & Garrod (2020) employed a modified-rate method approach introduced in Garrod (2008), demonstrating that appreciable COM production can occur even in the absence of diffusive chemistry.

As mentioned earlier, astrochemical models must be adaptable and flexible to accurately simulate chemistry across various astrochemical environments by incorporating both diffusive and non-diffusive chemistry. The inclusion of non-diffusive chemical processes is crucial for modeling colder regions more accurately, whereas hotter regions require special consideration of surface chemistry as well. If surface molecules are assumed to be bound solely by weak van der Waals forces, the efficiency of any significant surface chemistry becomes negligible. Acharyya et al. (2020) introduced the concept of chemisorbed sites, where molecules exhibit higher binding energies, thereby enabling surface chemistry even at temperatures exceeding 100 K.

To address these challenges, we introduce Pegasis, a fast and flexible three-phase astrochemistry code that incorporates both diffusive and non-diffusive grain-surface processes, along with all fundamental ice chemistry mechanisms applicable across diverse astrochemical environments. In this paper, we apply Pegasis to investigate the role of both diffusive and non-diffusive grain-surface processes in shaping the gas-phase and grain-surface chemical compositions of cold cores, specifically targeting the Cyanopolyyne peak position (TMC-1 (CP)) in the Taurus Molecular Cloud, given its ever-expanding and chemically rich inventory. Recent detections include several oxygen-bearing complex organic molecules—such as propenal (C_2H_3CHO), vinyl alcohol (C_2H_3OH), methyl formate ($HCOOCH_3$), and dimethyl ether (CH_3OCH_3) as reported by Agúndez et al. (2021), and ethanol (CH_3CH_2OH), acetone (CH_3COCH_3), and propanal (C_2H_5CHO) by Agúndez et al. (2023). Additionally, other newly identified species include 1,4-pentadiyne ($HCCCH_2CCH$; Fuentetaja et al. 2024), sulphur radicals (Cernicharo et al. 2024a), dinitriles (Agúndez et al. 2024), polycyclic aromatic hydrocarbons (PAHs) (Cernicharo et al. 2024b; Wenzel et al. 2024), thioacetaldehyde (CH_3CHS; Agúndez et al. 2025), the 1-cyano propargyl radical (HCCCHCN; Cabezas et al. 2025), and cyclopropenethione (c-C_3H_2S; Remijan et al. 2025).

The structure of the paper is as follows: In Section 2, we describe our model and the chemical processes it includes. Section 3 presents a benchmark comparison of Pegasis with the public version of Nautilus (Ruaud et al. 2016). In Section 4, we examine the differences between the three-phase chemistry prescriptions of Ruaud et al. (2016) and Hasegawa & Herbst (1993b), and compare the predicted gas-phase abundances with observations in TMC-1 (CP), considering both diffusive and non-diffusive chemistry. While a large number of species have been detected in TMC-1, we restrict our discussion to those included in the 2024 KIDA chemical network. Additionally, we compare the ice abundances with those observed in more evolved sources to gain insights into the transformation of the chemical inventory from cold cores to later evolutionary stages. Finally, we summarize our conclusions in Section 5.

---

[2] `https://github.com/smaret/astrochem`
[3] `https://astrochem-tools.org/codes/`
[4] `https://uclchem.github.io/`
[5] `https://github.com/fjdu/chempl`

2. Model description

Pegasis is a three-phase model (gas, grain-surface and grain-mantle) which presents a comprehensive and flexible approach towards understanding how molecular abundances evolve in the interstellar medium. The code has been designed to study the chemistry of molecular clouds, but it can also be easily extended to model chemistry in other evolutionary stages, such as protostars and protoplanetary disks. Following Ruaud et al. (2016), we let chemical reactions occur in the mantle as well as on the grain surface, albeit with a smaller rate of diffusion. This is implemented by setting the diffusion barrier for surface species as a smaller fraction of the binding energies (Garrod & Herbst 2006) than for mantle species. The interaction between grain surface and gas-phase chemistry occurs through accretion and desorption processes. Desorption can occur by thermal, non-thermal, or chemical mechanisms. For the three-phase chemistry, we implement prescriptions from both Ruaud et al. (2016) and Hasegawa & Herbst (1993b). Most of the processes are implemented as switches, allowing their effects to be explored separately. We use the most recent release from the KInetic Database for Astrochemistry (KIDA) (Wakelam et al. 2024) as our base chemical network. This includes 7667 gas-phase reactions and 4837 grain-surface and grain-mantle reactions and processes. Pegasis is implemented entirely in Python and is accelerated by Numba (Lam et al. 2024). Finally, the differential equations are solved using the the `DLSODES` solver from the `ODEPACK` library (Hindmarsh 1983) wrapped as a Python extension[6].

2.1. Modeling chemical processes

Pegasis employs a chemical kinetics-based approach to model different chemical processes, starting from a given set of initial conditions and evolving a system of coupled differential equations in time. The initial conditions define the physical and chemical configuration of the model, along with the starting concentrations of the molecules to be considered. In the simplest scenario, only the interstellar elemental abundances are used initially. The rate coefficients of each reaction are calculated and used to determine the total production or destruction of each species in the simulation.

For each species considered, Pegasis solves a system of ordinary differential equations involving each of the chemical species that may exist in the three phases of gas, grain surface and grain mantle. These equations describe the evolution of the abundance of species with time and take the form

$$
\begin{aligned}
\left.\frac{dn_{\mathrm{g}}(p)}{dt}\right|_{\mathrm{tot}} = &\sum_q \sum_r k_{qr} n_{\mathrm{g}}(q) n_{\mathrm{g}}(r) \\
&+ k^{\mathrm{g}}_{\mathrm{diss}}(q) n_{\mathrm{g}}(q) + k_{\mathrm{des}}(p) n_{\mathrm{s}}(p) \\
&- k^{\mathrm{g}}_{\mathrm{diss}}(p) n_{\mathrm{g}}(p) - k_{\mathrm{acc}}(p) n_{\mathrm{g}}(p) \\
&- n_{\mathrm{g}}(p) \sum_r k_{pq} n_{\mathrm{g}}(q),
\end{aligned}
\tag{1}
$$

$$
\begin{aligned}
\left.\frac{dn_{\mathrm{s}}(p)}{dt}\right|_{\mathrm{tot}} = &\sum_q \sum_r k^{\mathrm{s}}_{qr} n_{\mathrm{s}}(q) n_{\mathrm{s}}(r) \\
&+ k^{\mathrm{s}}_{\mathrm{diss}}(q) n_{\mathrm{s}}(q) + k_{\mathrm{acc}}(p) n_{\mathrm{g}}(p) \\
&+ k^{\mathrm{m}}_{\mathrm{swap}}(p) n_{\mathrm{m}}(p) + \left.\frac{dn_{\mathrm{m}}(p)}{dt}\right|_{\mathrm{m}\to\mathrm{s}} \\
&- n_{\mathrm{s}}(p) \sum_q k^{\mathrm{s}}_{pq} n_{\mathrm{s}}(q) \\
&- k^{\mathrm{s}}_{\mathrm{diss}}(p) n_{\mathrm{s}}(p) - k_{\mathrm{des}}(p) n_{\mathrm{s}}(p) \\
&- k^{\mathrm{s}}_{\mathrm{swap}}(p) n_{\mathrm{s}}(p) - \left.\frac{dn_{\mathrm{s}}(p)}{dt}\right|_{\mathrm{s}\to\mathrm{m}},
\end{aligned}
\tag{2}
$$

$$
\begin{aligned}
\left.\frac{dn_{\mathrm{m}}(p)}{dt}\right|_{\mathrm{tot}} = &\sum_q \sum_r k^{\mathrm{m}}_{qr} n_{\mathrm{m}}(q) n_{\mathrm{m}}(r) \\
&+ k^{\mathrm{m}}_{\mathrm{diss}}(q) n_{\mathrm{m}}(q) \\
&+ k^{\mathrm{s}}_{\mathrm{swap}}(p) n_{\mathrm{s}}(p) + \left.\frac{dn_{\mathrm{s}}(p)}{dt}\right|_{\mathrm{s}\to\mathrm{m}} \\
&- n_{\mathrm{m}}(p) \sum_q k^{\mathrm{m}}_{pq} n_{\mathrm{m}}(q) \\
&- k^{\mathrm{m}}_{\mathrm{diss}}(p) n_{\mathrm{m}}(p) \\
&- k^{\mathrm{m}}_{\mathrm{swap}}(p) n_{\mathrm{m}}(p) - \left.\frac{dn_{\mathrm{m}}(p)}{dt}\right|_{\mathrm{m}\to\mathrm{s}}.
\end{aligned}
\tag{3}
$$

Here k_{pq}, k^{s}_{pq} and k^{m}_{pq} are the rate coefficients in the gas phase, grain surface and grain mantle respectively between species p and q. k_{diss} is the rate for photodissociation processes, both in the gas phase and in the surface (s) and mantle (m) phases. Freeze-out (k_{acc}) of gaseous molecules onto the surface, and desorption (k_{des}) returning surface species to the gas are included. Transfer of material from the surface to the mantle and vice versa is included with a rate k^{s}_{swap} and k^{m}_{swap} respectively. Note that this swapping does not represent the actual movement of material across ice layers (Hasegawa & Herbst 1993b; Garrod & Pauly 2011; Ruaud et al. 2016).

For the reactions involving two reactants (bimolecular reactions), the rate coefficient is calculated using the modified Arrhenius formula (Kooij 1893)

$$
k = \alpha (T/300)^{\beta} \exp(-\gamma/T) \tag{4}
$$

For bimolecular reactions involving charged species, we follow Wakelam et al. (2012) and implement the temperature-dependent modification of rate coefficients using the Su-Chesnavich capture approach discussed in Woon & Herbst (2009). We suggest going through Wakelam et al. (2012, 2024) and references therein for more information on the kinds of bimolecular reactions included in the network. The charged gas-phase species can also react with negatively-charged dust grains in a neutralization reaction, with a rate coefficient given by

$$
k = \alpha \left(\frac{T}{300} \right)^{\beta} \tag{5}
$$

Here the activation energy γ is set to zero since this kind of recombination reaction is considered barrierless (Geppert & Larsson 2008). The 2024 KIDA network does not include positively-charged grains, thus processes such as collisional charging of grains as discussed in Draine & Sutin (1987) and collisions of positively and negatively charged grains as explored in Umebayashi (1983) are not included in our model.

---

[6] `https://github.com/kmaitreys/pylsodes`

The rate coefficient for processes involving ionization or dissociation by cosmic rays in the gas phase is given by the standard scaling relation (Semenov et al. 2010; Wakelam et al. 2012)

$$k_{\rm CR} = \alpha \zeta_{\rm CR} \tag{6}$$

where $\zeta_{\rm CR}$ is the cosmic-ray ionization rate for molecular hydrogen and the value of α is molecule dependent.

Cosmic rays can electronically excite both molecular and atomic hydrogen. The subsequent relaxation of these excited species produces UV photons, which can then dissociate or ionize molecules (Prasad & Tarafdar 1983). This CR-induced UV photodissociation/photoionization can occur in both the gas phase and on the grain surface, with a rate coefficient calculated as (Gredel et al. 1987, 1989; Gredel 1990; Sternberg et al. 1987)

$$k_{\rm UVCR} = \frac{\alpha}{1-\omega}\frac{n({\rm H_2})}{(n({\rm H})+2n({\rm H_2}))}\zeta_{\rm CR} \tag{7}$$

where ω, the albedo of grains in the far-ultraviolet, is taken as 0.5 (Wakelam et al. 2012).

For photodissociation caused by interstellar or stellar UV photons, the rate coefficient is given by

$$k_{\rm UV} = \alpha \exp{(-\gamma A_V)}\, F_{\rm UV} \tag{8}$$

in both the gas and the grain surface. Here, A_V is the visual extinction and $F_{\rm UV}$ the far-ultraviolet flux in Draine units. Ionization of molecules on the grain surface is not considered.

Instead of relying on a full radiative transfer for consideration of shielding from abundant gas phase species like H_2 and CO, we adopt the approximation suggested in Lee et al. (1996), where the photodissociation rates are calculated as a function of the visual extinction (A_V) and column densities of the H_2. For CO, we take shielding functions from Visser et al. (2009) and for N_2, we adopt the prescription from Li et al. (2013).

The gas phase and grain surface chemistry is linked through processes of accretion (adsorption) and desorption of the molecules. Only neutral molecules undergo adsorption and thus there is no charged surface species in the chemical network. Dust grains are assumed to be spherical and their size and material density can be set by the user. The rate constant for this process is given as (Semenov et al. 2010; Wakelam et al. 2012)

$$k_{\rm acc} = \pi\eta r_d^2\sqrt{\frac{8k_BT_g}{\pi m_p}}n_d \tag{9}$$

where m_p is the atomic mass of the species p and η is the sticking efficiency, which is taken as 100% for neutral species. The 2024 KIDA network does not contain charged species on grains, so efficiency for them is taken to be zero.

In sufficiently warm regions, molecules can evaporate thermally from the grain surfaces and rate constant for this process is given by the first-order Polanyi-Wigner equation (Katz et al. 1999; Herbst et al. 2005; Semenov et al. 2010)

$$k_{\rm des} = \nu_0(p)\exp\left(\frac{-E_d}{T_d}\right) \tag{10}$$

where $\nu_0(p)$ is the characteristic frequency of species p on the grain surface, approximated as a harmonic oscillator relation

$$\nu_0(p) = \sqrt{\frac{2n_sE_d}{\pi^2 m_{\rm H} m_p}} \tag{11}$$

by Tielens & Allamandola (1986) and Hasegawa et al. (1992). Here, E_d is the adsorption energy of H. Unlike Collings et al. (2004), thermal evaporation in our model only involves the topmost layer in the sense we do not consider multilayer thermal desorption. We also consider desorption driven by cosmic rays following Hasegawa & Herbst (1993a).

For photo-desorption driven by standard interstellar UV photons, we have the rate formula (Ruaud et al. 2016; Wakelam et al. 2021)

$$k_{\rm UV,des} = F_{\rm UV}S_{\rm UV}\exp{(-2A_V)}\,Y_{\rm pd}\frac{4\pi r_d^2}{N_s} \tag{12}$$

and for secondary UV photons induced by cosmic rays, we have

$$k_{\rm UVCR,des} = F_{\rm UVCR}S_{\rm UVCR}Y_{\rm pd}\frac{4\pi r_d^2}{N_s} \tag{13}$$

The yield $Y_{\rm pd}$ is taken as 10^{-4} molecules per photon following Andersson & van Dishoeck (2008). F is the strength of the UV field in Draine units and S is the corresponding scaling factor. For standard interstellar UV, we take $F_{\rm UV} = 10^8$ photons cm^{-2} s^{-1} (Öberg et al. 2007) with $S_{\rm UV} = 1$ and for cosmic ray induced UV, we take $F_{\rm UVCR} = 10^4$ photons cm^{-2} s^{-1} (Shen et al. 2004) with $S_{\rm UVCR} = \zeta/1.3\times10^{17}$, ζ being the H_2 cosmic ray ionization rate. The factor of 2 in equation (12), accounts for the extinction of UV photons relative to the visual extinction A_V (Roberge et al. 1991).

The chemical reactions proceeding on the grain surfaces can be exothermic which in turn can trigger desorption of a molecule to gas phase. In our model, we implement two modes of chemical desorption. The first mode is based on the work of Garrod et al. (2007), which is based in the Rice-Ramsperger-Kessel (RRK) theory (see Holbrook et al. 1996). We define f to be the probability that a given reaction results in desorption because of this exothermicity as

$$f = \frac{\nu P}{\nu_s + \nu P} = \frac{aP}{1+aP} \tag{14}$$

where $a = \nu/\nu_s$ is the ratio of surface-molecule bond frequency to the frequency at which energy is lost to the grain surface. The RRK probability P is given by

$$P = \left(1-\frac{E_d}{E_{\rm reac}}\right)^{s-1} \tag{15}$$

where E_d is the desorption energy of the molecule being desorbed to gas phase, $E_{\rm reac}$ is the enthalpy of formation for the reaction and s is the number of vibrational modes in the molecule-surface bond system. For diatomic species, $s = 2$ and for all others, $s = 3\mathcal{N}/5$, with $\mathcal{N}$ being the total number of atoms in the desorbing molecule.

The second mode is based on the experimental work of Minissale et al. (2016) and its extension in Riedel et al. (2023). We adopt experimental values for the evaporation fraction for reactions involving H and OH ($f = 0.25$), O and H ($f = 0.3$) and N and N ($f = 0.5$) as reactants from Minissale et al. (2016). For the rest of reactions, the general expression of evaporation fraction is given by

$$f = \exp\left(-\frac{\mathcal{F}E_d}{\epsilon E_{\rm reac}}\right) \tag{16}$$

Here, ϵ is fraction of kinetic energy produced in the exothermic reaction retained by the reaction product. $\mathcal{F}$ is the the degrees of freedom of the product and is taken as $\mathcal{F} = 3\mathcal{N}$. The expression for ϵ can be written as

$$\epsilon = \left(\frac{M - m}{M + m}\right)^2 \tag{17}$$

where M is the effective mass of the surface component and m is the mass of the reaction product which receives this kinetic energy. Because the surfaces involved can vary, being covered by ices of different species, we adopt values of effective surface mass M from Vasyunin et al. (2017). We consider three possibilities: a water ice substrate (M = 48 u), a CO ice substrate (M = 100 u) and finally, bare grains where number of surface layers is less than or equal to unity (M = 120 u). Every surface that is not covered with water ice or is not a bare grain is assumed to be covered with CO ice (Riedel et al. 2023). Note that, in the case of just one reaction product, this process involves two bodies (one desorbing product and the surface component). In the reactions with two desorbing products, we accordingly modify the expression for $\mathcal{F}$ accordingly to include contribution of the second product. Finally, the total time-dependent evaporation fraction is given as (Riedel et al. 2023)

$$f(i,t) = \sum_j f_j(i) \cdot \frac{n^\star_j(t)}{n^\star_{\rm surf}(t)} \tag{18}$$

where $f_j(i)$ is the individual fraction for the three surface types (bare grain, H_2O and CO), $n^\star_j$ is the surface sites populated by surface type j and $n^\star_{\rm surf}$ is the total surface site abundance.

Finally, we implement the non-thermal desorption mechanism introduced by Wakelam et al. (2021), in which the sputtering of icy grain material due to incoming cosmic ray bombardment is considered. This process allows mantle species to desorb directly into the gas phase without passing through the surface layers.

Accreted molecules can undergo diffusive reactions via the Langmuir-Hinshelwood (L-H) mechanism. We consider the competition between diffusion, evaporation, and reaction itself, following Ruaud et al. (2016). In this mechanism, molecules are physisorbed, meaning that weaker van der Waals forces (Reboussin et al. 2014) enable diffusion to occur more readily (Vidali et al. 2006).

Physisorbed molecules can diffuse from one site (which is essentially a potential well) to other in multitude of ways depending on their size. All molecules can undergo thermally driven diffusion on a time scale given as (Hasegawa et al. 1992; Semenov et al. 2010)

$$t_{\rm hop} = \frac{1}{\nu_0} \exp\left(\frac{E_b}{T_d}\right) \tag{19}$$

where T_d is the grain temperature. Following Hasegawa et al. (1992), we also allow the species to undergo diffusion through quantum tunneling and the time scale $t_{\rm qt}$ for this process is

$$t_{\rm qt} = \frac{1}{\nu_0} \exp\left(\frac{2a}{\hbar}\sqrt{2mE_b}\right) \tag{20}$$

where a is the diffusion barrier thickness and E_b is the potential energy barrier between two adjacent surface sites. Further, we also implement cosmic ray-induced diffusion following Kalvāns (2014).

2.2. Three-phase chemistry

We implement both the prescriptions for three-phase chemistry from Ruaud et al. (2016) and Hasegawa & Herbst (1993b) which can be switched with each other as per user's discretion. In Ruaud et al. (2016) (hereafter RWH16), when a molecule is lost at the surface, it is immediately replaced by transferring a molecule from the mantle to the surface, whereas in Hasegawa & Herbst (1993b) (hereafter HH93), the vacant site remains as is until the determination of the next accretion or desorption event. If the type of event is accretion, then the vacant site is filled in with a newly adsorbed molecule, and if it is a desorption event, then the vacant site is filled in with a molecule from the mantle. More formally, the net rate of change in total surface material can be written as

$$\frac{dn_{\rm s,tot}}{dt} = \frac{dn_{\rm s,gain}}{dt} + \frac{dn_{\rm s,loss}}{dt} \tag{21}$$

Pertaining to this, in HH93, we have

$$\text{If} \quad \frac{dn_{\rm s,tot}}{dt} > 0 \begin{cases} \left.\dfrac{dn_{\rm s}(p)}{dt}\right|_{\rm s\to m} = \alpha_{\rm gain}\dfrac{n_{\rm s}(p)}{n_{\rm s,tot}}\dfrac{dn_{\rm s,tot}}{dt} \\ \left.\dfrac{dn_{\rm m}(p)}{dt}\right|_{\rm m\to s} = 0 \end{cases} \tag{22}$$

and

$$\text{If} \quad \frac{dn_{\rm s,tot}}{dt} < 0 \begin{cases} \left.\dfrac{dn_{\rm s}(p)}{dt}\right|_{\rm s\to m} = 0 \\ \left.\dfrac{dn_{\rm m}(p)}{dt}\right|_{\rm m\to s} = \alpha_{\rm loss}\dfrac{n_{\rm m}(p)}{n_{\rm m,tot}}\dfrac{dn_{\rm s,tot}}{dt} \end{cases} \tag{23}$$

Evidently, RWH16 considers accretion at the surface of grains is a random process; the incoming molecule adsorbs randomly at the surface and the molecule located below the vacant site is immediately available for desorption.

2.3. Non-diffusive chemistry

In order to explain the observations of COMs in cold cores, several authors have proposed alternative formation pathways on grain surfaces without solely relying on diffusive chemistry. Ruaud et al. (2015) introduced the Eley-Rideal (E-R) mechanism and formation of the van der Waals complexes on grain surfaces in addition to standard diffusive chemistry. More recently, Jin & Garrod (2020) formalized several mechanisms further that can proceed through non-diffusive grain chemistry. In the standard L-H diffusive chemistry formalism of Hasegawa et al. (1992), the complete rate equation can be written as

$$R^{pq}_{\rm diff} = \kappa_{pq}(k^p_{\rm hop} + k^q_{\rm hop})\frac{n(p)n(q)}{N_s n_d} \tag{24}$$

where $k_{\rm hop} = 1/t_{\rm hop}$ is the hopping rate (thermal or quantum mechanical tunneling, whichever is faster) with $n(p)$ and $n(q)$ being the abundances of reactants p and q. In a similar fashion, we adopt the following general expression for the reactions proceeding with through the non-diffusive mechanisms (Jin & Garrod 2020)

$$R^{pq}_{\rm nd} = \kappa_{pq}R^p_{\rm cmp}\frac{n(q)}{N_s n_d} + \kappa_{pq}R^q_{\rm cmp}\frac{n(p)}{N_s n_d} \tag{25}$$

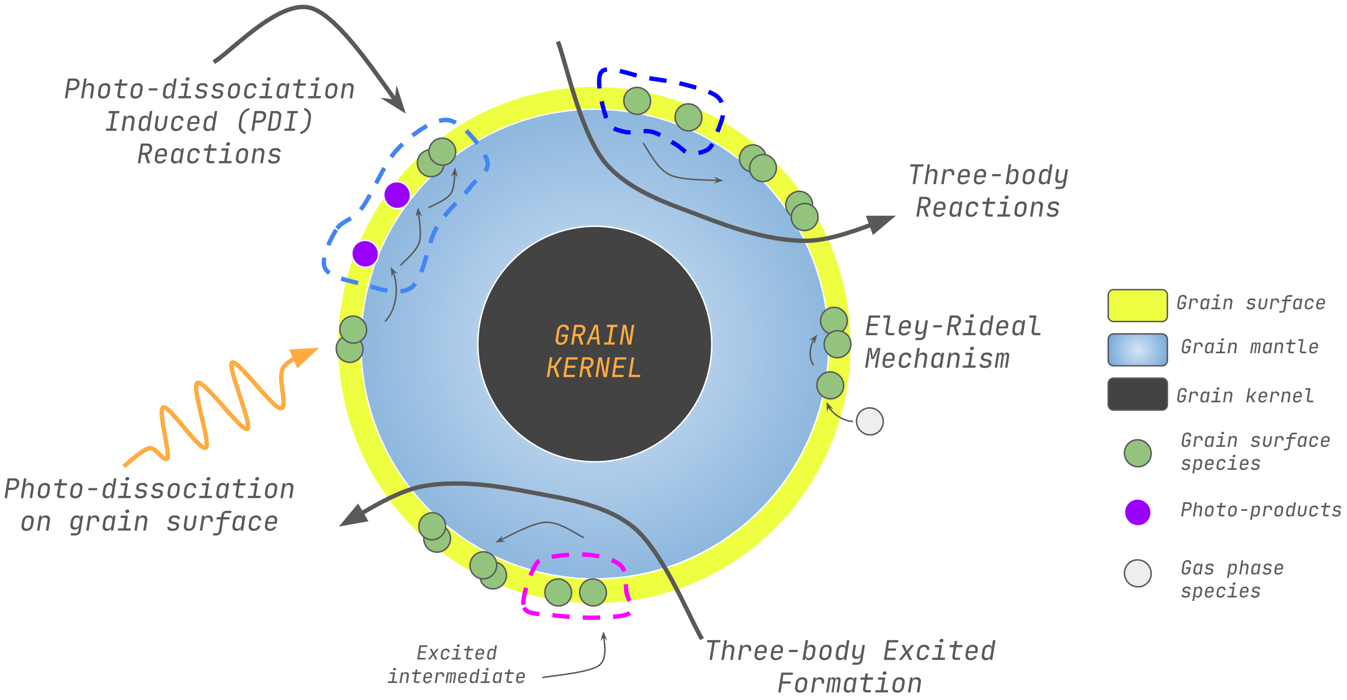

Fig. 1. A schematic depicting all non-diffusive chemistry processes included in Pegasis.

Here, we have defined $R^i_{\rm cmp}$ as the completion rate of the reaction which corresponds to the appearance rate of species i. For diffusive chemistry, $R^i_{\rm cmp} = k^i_{\rm hop} n(i)$ and equation (25) simply reduces to equation (24). The expression for $R^i_{\rm cmp}$ is dependent on the specific non-diffusive mechanism. All non-diffusive mechanisms are depicted through the schematic in Figure 1 and Appendix A describes how the reaction network for non-diffusive reactions was generated from the 2024 KIDA network.

Table 1. Description of the processes included in each model presented in this work.

Model	Three-phase prescription	Non-diffusive chemistry
M1	RWH16	No
M2	HH93	No
M3	RWH16	Yes
M4	HH93	Yes

2.4. Chemisorption

So far, in all the chemical processes considered, the surface species were physisorbed from the gas-phase onto the grain surface. As discussed earlier, molecules are bound to physisorption sites via weak electrostatic forces which make them susceptible to desorptive processes in high temperature environments ($>$ 100 K). To study the effects of surface chemistry at these temperatures, we include a new variant of surface species in our model as they behave differently than the species which undergo physisorption. This different labeling comes as a consequence of treating physisorption and chemisorption sites differently, with the difference originating due to the different binding energies with which the molecules bind to the surface (Cazaux & Tielens 2002). Like non-diffusive chemistry, various mechanisms through which chemisorption can occur are considered and the formulation is primarily based on the work of Acharyya et al. (2020) from where we also get the reaction set for each of those mechanisms.

Similar to diffusive reactions via physisorption sites, we allow surface reactions as well as reactive desorption processes through the chemisorbed sites in mostly an identical manner. Like all mechanisms under chemisorption, these rates are only calculated when the grain temperature is above 100 K. We implement all the processes as described for physisorbed species so far for each of the diffusive chemistry reaction of the chemisorbed species included in our network. In summary, all chemical processes (except non-diffusive chemistry) involving grain-surfaces and grain-mantles are depicted in the schematic in Figure 2.

3. Benchmarking PEGASIS

We benchmark Pegasis with the public version of Nautilus used in RWH16. We ran both codes for same physical conditions and switches for the 2014 and 2024 releases of the KIDA network. Note that because many processes such as non-diffusive chemistry and chemisorption are unique to Pegasis, these have been excluded from our comparison models. To this end, we adopt typical cold core conditions for our physical parameters. The gas number density is taken as $n_{\rm H} = 3 \times 10^4$ cm^{-3}. We assume a temperature of 10 K for both gas and grains and a visual extinction of 15 mag. The standard cosmic ionization rate $\zeta_{\rm H_2}$ of 1.3×10^{-17} s^{-1} was assumed. Additionally, we allow photodesorption and self-shielding for H_2, CO and N_2. Quantum tunneling is not considered in this comparison; only thermal diffusion

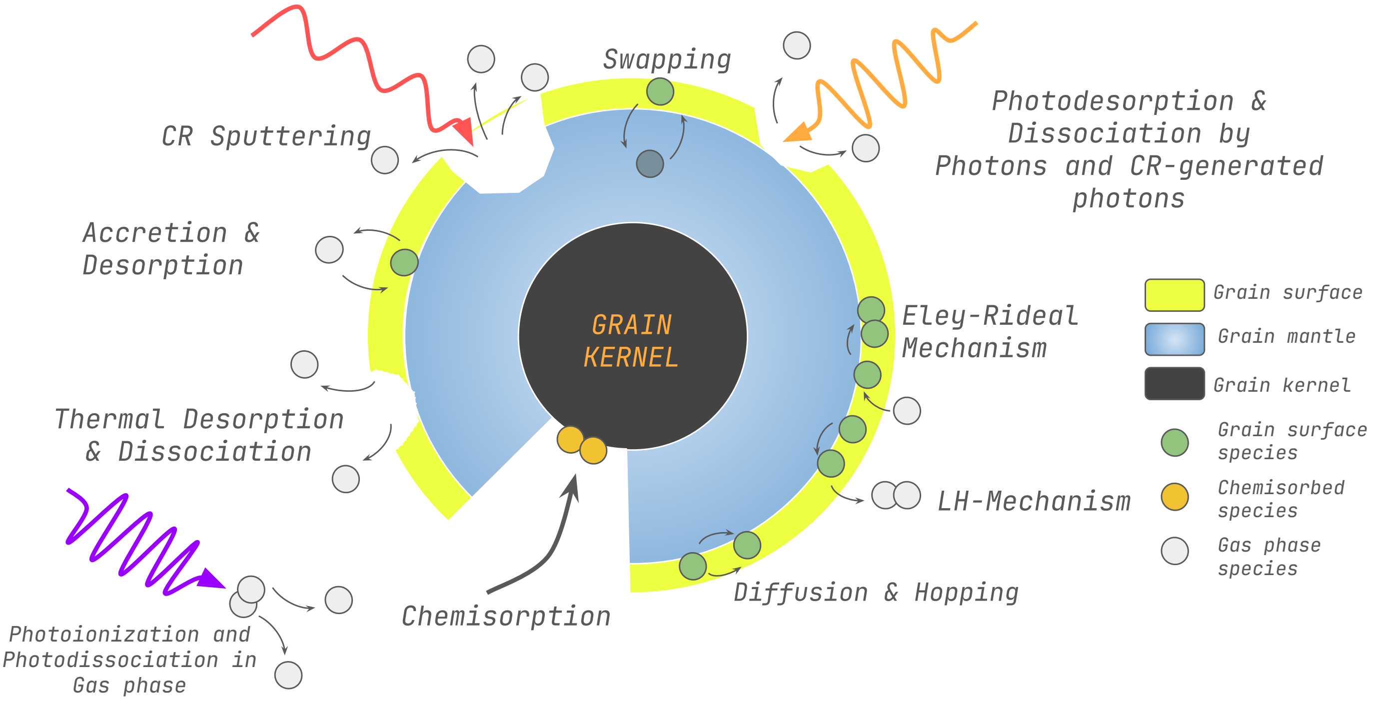

Fig. 2. A schematic depicting all ice chemistry processes (except non-diffusive chemistry) included in Pegasis.

being possible. Spherical grains of radius 0.1μm and density 3 g cm^{-3}, with a dust-to-gas mass ratio of 0.01 were assumed. Following RWH16, 10^6 surface sites per grain were assumed and the ratio of diffusion barrier to binding energy is taken to be 0.4 for surface species and 0.8 for mantle species. Initial elemental abundances are taken from RWH16. We run all models for 1 Myr.

We take this opportunity to also use our model to investigate differences between the 2014 and 2024 releases of the KIDA chemical network for key species. The comparison is further discussed in Appendix B. As evident from this benchmarking, Pegasis and Nautilus show excellent agreement for identical initial conditions and chemical networks used to simulate cold core conditions.

4. Model predictions using different approaches

To explore the different mechanisms used in the literature to simulate three-phase chemistry and to consider the effect of non-diffusive chemistry, we consider four different cold dense cloud models (Table 1). The motivation is to find the model providing the best agreement with observed abundances in TMC-1. The physical conditions assumed are from Fuente et al. (2019) with gas number density $n_H = 3 \times 10^4$ cm^{-3}, gas and grain temperatures = 10 K, visual extinction A_V = 15 mag and ζ_{H_2} = 1.3×10^{-17} s^{-1}. Following Wakelam et al. (2024), we take a larger value of 2.5 Å for the diffusion barrier thickness than was assumed in the benchmark models. Once again, spherical grains of radius 0.1μm with 3 g cm^{-3} material density are assumed, with a dust-to-gas mass ratio of 0.01. A surface site density of 1.5×10^{15} cm^{-2} is assumed. Following RWH16, the ratio of diffusion barrier to binding energy is taken as 0.4 for the surface and 0.8 for the mantle. We let all species to diffuse thermally as well as through quantum tunneling. Photodesorption and cosmic-ray sputtering is also enabled for all models. For chemical desorption, we use the prescription from Riedel et al. (2023) as it accounts for the nature of the desorbing surface. Finally, the initial elemental abundances are taken in atomic form from Vidal et al. (2017) (except for hydrogen, which is assumed to be converted entirely into molecular form at the beginning) and all models are run for 10 Myr.

4.1. Comparing three-phase chemistry prescriptions

In this section, we explore the effect of the two three-phase chemistry prescriptions on the growth of ices and how non-diffusive chemistry can further influence the contribution of different species. Figure 3 shows the total number of layers formed by major ices for each model included in this work. The total number of layers is calculated by dividing the ice concentrations (for both surface and mantle) with the total number of sites available per gas phase molecule. We note that, the original implementation of HH93 did not consider active mantle chemistry, but for all our models, mantle species participate in all possible chemical reactions and photoprocesses.

Both three-phase prescriptions show a very similar distribution of major ices. H_2O and CO ices are the most dominant, making up bulk of the ice thickness. We observed that the diffusive models with both the three-phase prescriptions of RWH16 and HH93 produced similar amount of ice layers, although the share across different ice species is notably different. There is much more CH_4 ice in M1 as compared to M2, and the CO abundance does not decline after 1 Myr in case of M2, as it does for M1. Moreover, these trends are similar when non-diffusive chemistry is activated in M3 and M4 (see Section 4.4 for discussion). As noted earlier, in the case of RWH16, molecules are im-

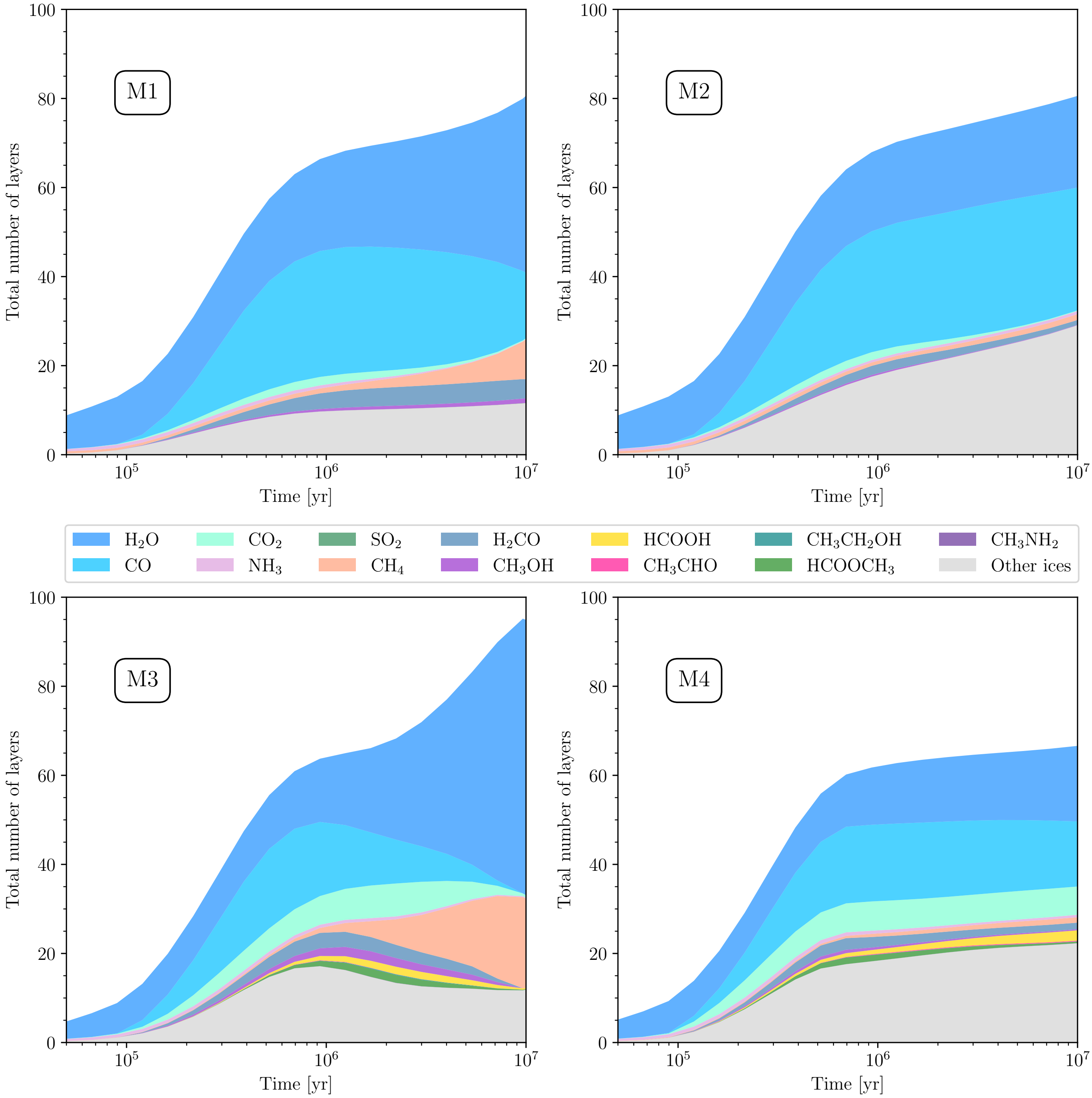

Fig. 3. Evolution of ice thickness represented as the total number of layers across major ice species for all the models. The contributions were calculated by accounting for the abundances of both surface and mantle species. The top row is for models with diffusive chemistry and the bottom row for the models with non-diffusive chemistry.

mediately available for desorption as soon as the molecule above them leaves the surface, independent of the next event.

The individual contributions of major ices are sensitive to different chemical processes that can be included or excluded in a model run and the chemical network as they affect chemistry by altering dominant pathways of production of these ices. For instance, RWH16, discussed the effects of reaction diffusion competition on the ice thickness variability.

To investigate the differences between the two prescriptions more quantitatively, we looked into the evolution of surface layers and mantle layers individually over the simulation time (Figure 4) for models with and without non-diffusive chemistry. We note that the number of mantle layers evolves similarly for both prescriptions, but the surface layers saturate at different values. This is expected, as HH93 does not account for surface thickness, whereas RWH16 includes it by considering the two outermost layers as part of the surface, following Fayolle et al. (2011). In HH93, the active surface layers are modeled through the core

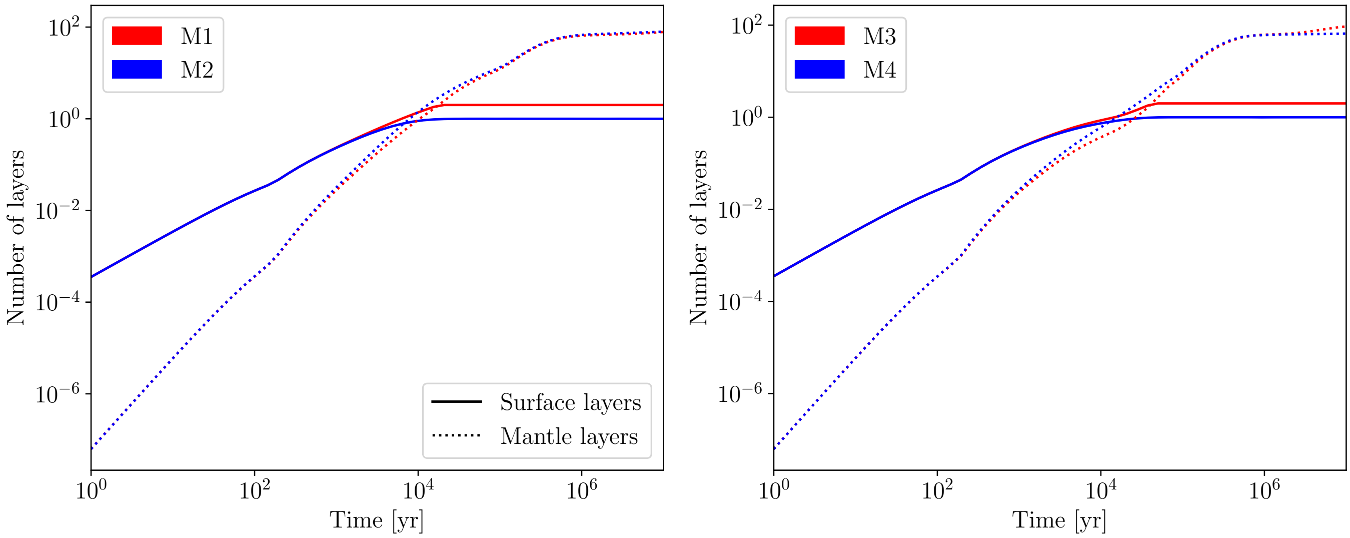

Fig. 4. Evolution of ice thickness as a function of number of surface and mantle layers individually for models without non-diffusive chemistry (left) and with non-diffusive chemistry (right).

coverage factor α

$$\alpha_{\text{gain}} = \frac{\sum_p n_s(p)}{N_{\text{site}}} \tag{26}$$

where the numerator represents the total surface abundance and N_{site} is the total number of sites on a grain. Another key difference between the two prescriptions is that the movement of material between grain surface and grain mantle is solely based on conservation of mass in the case of HH93, whereas RWH16 adopts the recommendation from Garrod (2013), where these rates are modeled through the thermal hopping (diffusion) time scales of the mantle molecules. Due to the absence of a buffer where outer monolayers are considered part of the surface in HH93, the heavier species are progressively trapped in the mantle. At late times, the accretion rates as well as desorption rates decrease as there is not enough material from gas phase to accrete on the grain surfaces. The species locked in mantle have longer desorption time-scales as they have to first transition to the surface. In addition, in case of HH93, the mantle to surface transitions are dependent on the desorption rates, and not the hopping rates, and these rates are much lower at late times when compared to RWH16. This affects the heavier species much more than the three lightest species, H, H_2 and He, which have low binding energies facilitating high desorption rates (Govers et al. 1980). In our models, we allow direct desorption from mantles through the process of cosmic-ray sputtering. This directly brings mantle species back to the gas phase, without them having to first move to the surface layer. For both prescriptions, as adsorption and desorption decline on the surface with time, species still move from the surface to the mantle, thus we observe saturation of surface abundances after $t > 10^5$ yr. In the case of RWH16, the surface roughness assumption provides a buffer for grain surface chemistry to proceed and saturate after completely filling up the outer active monolayers region. Finally, we briefly note the the two prescriptions produce significant differences for models with and without non-diffusive chemistry (models M3 and M4 in Figure 3) which are discussed in more detail in Section 4.4.

4.2. Gas compositions in TMC-1

In this section, we concentrate on reproducing the gas-phase chemical abundances observed in the well studied TMC-1 (CP) (Kaifu et al. 2004; Gratier et al. 2016; Agúndez & Wakelam 2013). All observations were derived in the form of column densities and then converted to abundances with respect to atomic hydrogen assuming $N(H_2) = 10^{22}$ cm^{-2} (Cernicharo & Guelin 1987; Gratier et al. 2016).

The models in Table 1 share the same physical and chemical conditions but differ in their choice of three-phase chemistry prescription and the inclusion or exclusion of non-diffusive chemistry. The goal is to determine which of the four models best reproduces the observations and to estimate the chemical age of the source (see, for instance, Majumdar et al. 2017). According to Smith et al. (2004) and Wakelam et al. (2024), abundances are considered well-reproduced if they fall within one order of magnitude of the observed value. There have been several statistical methods employed by various authors to get an estimation on how well an observation is reproduced by a model. Wakelam et al. (2024); Wakelam et al. (2010) employ the distance of disagreement method, where the best-fitting time corresponds to the minimum value of the parameter D

$$D(t) = \frac{1}{N_i} \sum_i \left| \log(X_{\text{mod},i}(t)) - \log(X_{\text{obs},i}) \right| \tag{27}$$

where $X_{\text{mod},i}(t)$ is the modeled abundance of species i at time t and $X_{\text{obs},i}$ is the observed abundance of species i from an observation dataset (Agúndez & Wakelam (2013) or Gratier et al. (2016)). This works well to get an estimate on the best-fitting time but is susceptible to (large) outliers and would be better suited if the uncertainties on all observations were readily available. The mean logarithmic differences approach from Loison et al. (2013) and Wakelam et al. (2015) suffers from a similar problem.

Instead, we use the mean confidence level approach discussed in Garrod et al. (2007), which works well for our case and has also been applied in Majumdar et al. (2017) and RWH16. For

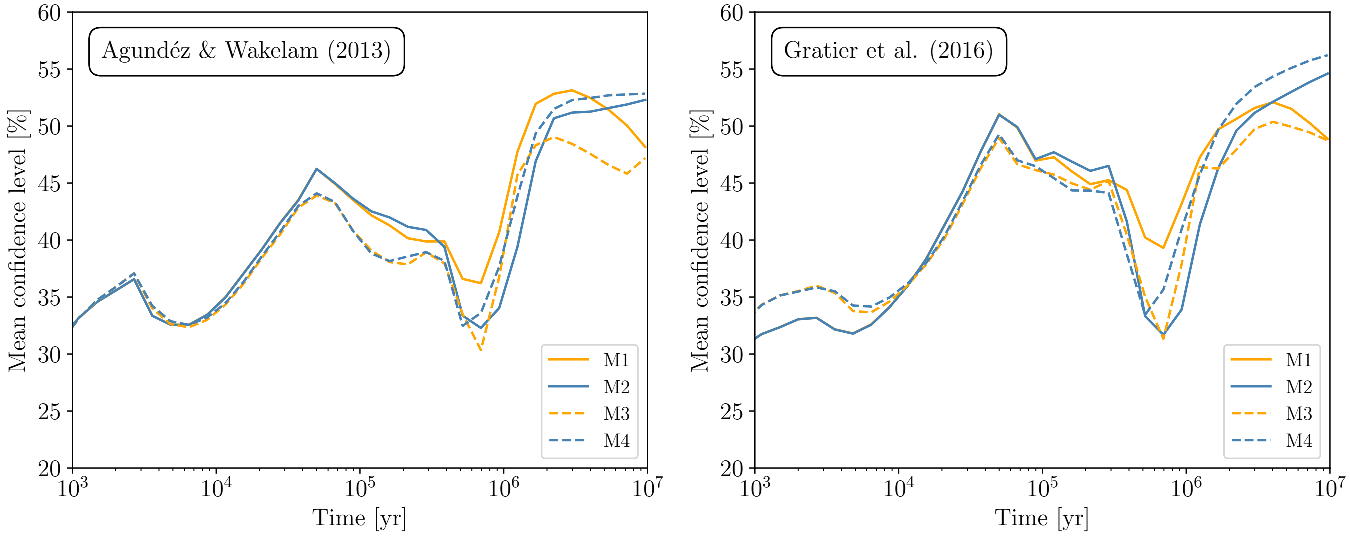

Fig. 5. Mean confidence level (%) for different models for fit with observations from the TMC-1 molecular cloud. The solid lines represent models without non-diffusive chemistry and dashed lines are models with non-diffusive chemistry.

this, we define confidence level κ_i as

$$\kappa_i = \mathrm{erfc}\left(\frac{\log(X_{\mathrm{mod},i}) - \log(X_{\mathrm{obs},i})}{\sqrt{2}\sigma}\right) \tag{28}$$

where erfc is the complementary error function and we take $\sigma = 1$ implying 1 standard deviation corresponds to the modeled value being within one order of the observed value following Garrod et al. (2007). We calculate κ_i for each species at each time and the overall confidence at each time is defined by taking the mean of the individual levels over all species. We plot the mean confidence level for each model in Figure 5 for both the observation datasets. For this analysis, we have considered all the models in Table 1 over a period of 10 Myr.

Our results are similar to the findings of Garrod et al. (2007) in that they produce two distinct local maximas for the mean confidence level, and therefore provide two choices for the best-fitting time. The first local maximum for all models with respect to both observation sets is much flatter and represents a considerably larger interval ranging from approximately 4×10^4 yr to 2×10^5 yr. On the other hand, the late times obtained for models M1 and M3 (few 10^6 yr) produce a greater mean confidence level value, though Hartquist et al. (2001) suggest that TMC-1 is a relatively young molecular cloud ($< 10^5$ yr for TMC-1 Core D). However, according to Hartmann et al. (2001) and Mouschovias et al. (2006), an age of a few 10^5 yr is too short as some estimates put the age of these dense clouds in the range of $10^6 - 10^7$ yr. In a more recent work, Navarro-Almaida et al. (2021) suggest that observations of TMC-1 (CP) can be best explained with a gravitational collapse model ($t \sim 1$ Myr) or a more sophisticated collapse model with ambipolar diffusion ($t \sim 10$ Myr). Nevertheless, we note that the late best-fitting times for models M1 and M3 are in agreement with the best times found by Wakelam et al. (2024). For the HH93 (M2 and M4) models we fail to find a definitive maximum at late times with either of the observational datasets of Agúndez & Wakelam (2013) or Gratier et al. (2016). For M1 and M3 (i.e., the RWH16 models), where we do observe a peak after 1 Myr, we note that the confidence level value for these late times exceed the value for early time.

The cases where we note the confidence still increasing beyond 10 Myr suggests at the limitations of our model. These limitations can be attributed to both the chemical network, as well as the individual chemical processes considered in our model. Moreover, our model is a pseudo-time-dependent, where the physical conditions remain constant through the evolution of the cloud. In reality, these environments are much more complex, with processes like turbulence, shocks and evolving densities due to core collapse affecting the chemical time-scales immensely. Therefore, in the cases where the statistical methods fail to produce the best time within the reasonable limits, authors such as Garrod et al. (2007) have opted to discard the models on physical and chemical grounds. The effects of non-diffusive chemistry in estimating chemical ages within the 10 Myr range is discussed in Section 4.4.

Overall, as evident from Figure 6, the RWH16 model M1, can reproduce the observed abundances for the most number of species, 23 out of 32 gas-phase species abundances for Gratier et al. (2016) and 47 out of 61 gas-phase species from Agúndez & Wakelam (2013) with best times of 4 Myr and 3 Myr respectively within a factor of ten. Note that while making Figure 6, any observations with lower or upper limits were not considered. Upon including them, M1 can reproduce 28 out of 37 gas-phase species abundances for Gratier et al. (2016) (with a confidence of 52%) and 48 out of 70 gas-phase species from Agúndez & Wakelam (2013) (with a confidence of 53%). The non-diffusive RWH16 model M3 also produces similar best-fitting times as M1, although with less mean confidence. HH93 models M2 and M4, despite producing even larger confidence (as high as 56% in case of M4) at late times, failed to attain a maximum within 10 Myr.

This ambiguity while trying to find the best-times is expected because of the complex structure of TMC-1 as well as the distinct physical history of its substructures. The time where the mean confidence attains a maximum is also susceptible to the initial conditions assumed, especially the starting C/O ratio (Agúndez & Wakelam 2013). The role of desorption mechanisms in estimating the chemical ages through modeling has been brought up several times (Herbst 1995, 2001; Garrod et al.

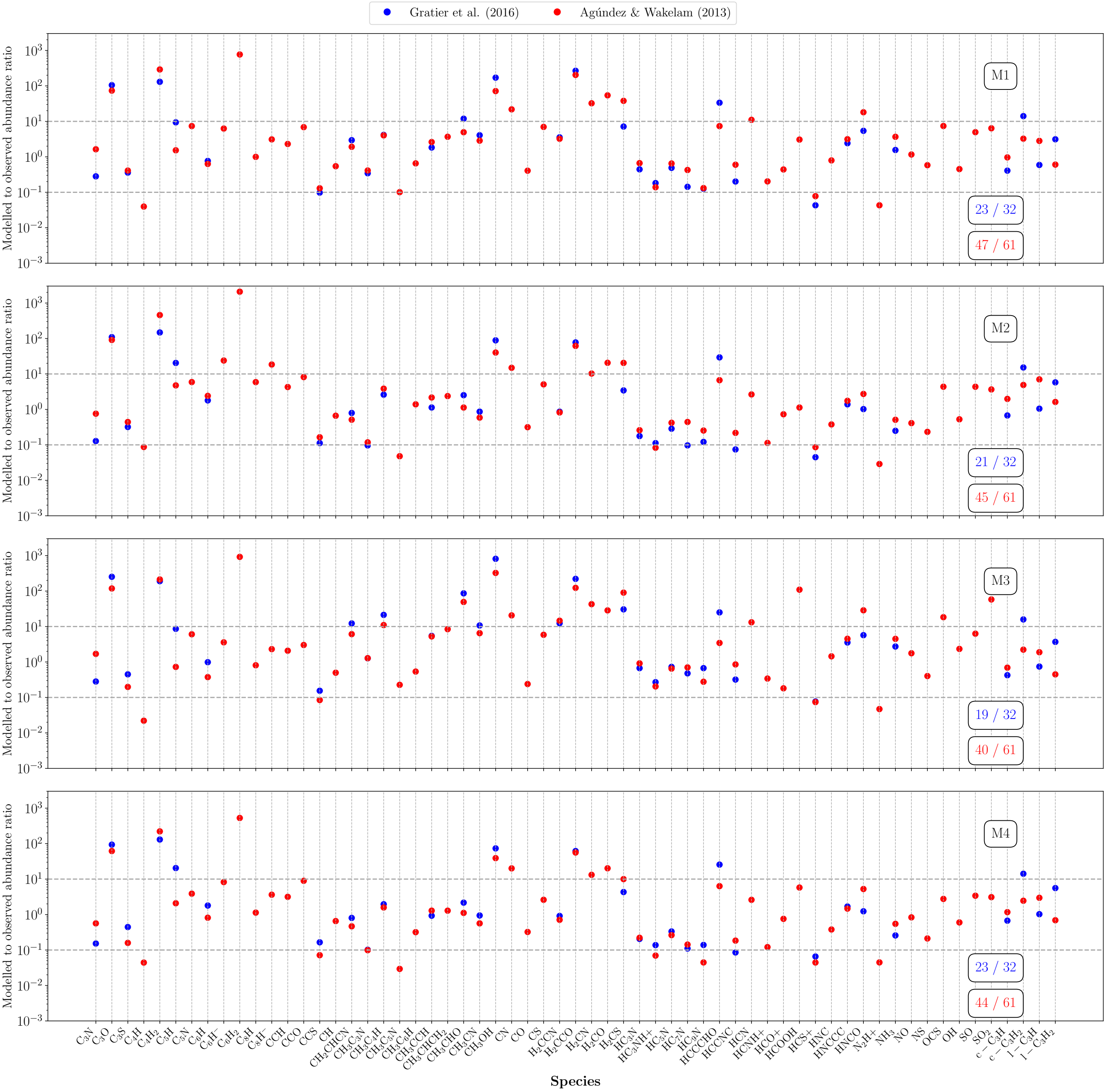

Fig. 6. The ratios of modeled abundances to observed abundances for both datasets used in this work for each model. Only species without any upper or lower limits are displayed here, with the number of species that each model could reproduce for the datasets of Gratier et al. (2016) (in blue) and Agúndez & Wakelam (2013) (in red).

2006). Finally, the networks can also affect the overall agreements with the observations and provide different best-fitting times (Wakelam et al. 2024).

4.3. Ice compositions

Ice compositions have been observed in absorption along the line of sight towards background stars, massive young stellar objects (MYSOs) and low-mass young stellar objects (LYSOs). Here we compare observations of these objects with our model predictions. We use the ice abundances at the best fit age for gas phase observations of TMC-1. The observations and model abundances (relative to those of water ice) are given in Table 2. We include both surface and mantle abundances in the model predictions. In addition to the interstellar sources, we also include the abundances from cometary bodies in our comparison.

In this section, we discuss the results of model M1 and M2 for major ices species. Models M3 and M4 which involve non-diffusive chemistry are discussed in the next section. Table 2 clearly shows that non-diffusive chemistry can significantly impact the contribution of different ice species to the total ice, the differences are evident between M1 and M3 and between M2

Table 2. Observed ice composition in various massive young stellar objects (MYSOs), low-mass young stellar objects (LYSOs), and background (BG) stars, along with a Kuiper belt comet, compared against model predictions at the best-fitting times determined using gas-phase abundances.

Ice species	$X_{\mathrm{H_2O}}$(%)				Literature (% H_2O)			
	M1	M2	M3	M4	BG Stars	MYSOs	LYSOs	Comets
$H_2O^{\star}$	9.28(−5)	6.95(−5)	1.16(−4)	5.71(−5)	100	100	100	100
CO	91.84	134.92	18.68	87.17	9–67(a)	3–26(a)	<3–85(a)	0.4–30(a,e)
CO_2	2.84	0.76	16.96	37.63	14–43(a)	11–27(a)	12–50(a)	4–30(a,e)
CH_4	12.70	6.36	32.53	7.12	<3(a)	1–3(a)	1–11(a)	0.4–1.6(a,e)
NH_3	0.86	3.37	1.38	3.35	<7(a)	∼7(a)	3–10(a)	0.2–1.4(a,e)
CH_3OH	2.93	0.45	3.98	1.59	<1–12(a)	<3–31(a)	<1–25(a)	0.2–7(a,e)
H_2CO	15.88	5.31	7.04	8.64	–	∼2–7(a)	∼6(a)	0.11–1.0(a,e)
HCOOH	5(−3)	3(−3)	4.24	13.69	<2(a)	<0.5–6(a)	<0.5–4(a)	0.06–0.14(a,e)
CH_3CHO	1(−3)	5(−5)	0.02	1.03	–	<2.3(b)	–	0.047(f,g)
C_2H_5OH	4(−4)	2(−4)	0.31	0.13	–	<1.9(b)	–	0.039(f,g)
$HCOOCH_3$	0.06	0.02	2.98	2.14	–	–	<2.3(c)	0.0034(f,g)
CH_3NH_2	0.01	1(−3)	0.08	0.19	–	<3.4(b)	<16(d)	–
SO_2	3(−5)	6(−10)	6(−4)	5(−3)	–	<0.9–1.4(a)	0.08–0.76(a)	0.2(a,e)

Notes. Model columns (M1–M4) represent specific simulation setups where $a(b) = a \times 10^b$, and the observation columns summarize results from different astronomical sources. Dash (–) indicates no data. The best-fitting times for models M1-M4 were 4 Myr, 9.64 Myr, 4 Myr and 9.64 Myr respectively.
(⋆) For H_2O, we have listed the abundance of total water ice with respect to gas-phase H for each model.

References. (a) Boogert et al. (2015), (b) Terwisscha van Scheltinga et al. (2018), (c) Terwisscha van Scheltinga et al. (2021), (d) Rachid et al. (2020), (e) Mumma & Charnley (2011), (f) Rocha et al. (2024), (g) Rubin et al. (2019).

and M4. The sources and objects considered in this section are more evolved than TMC-1 and have different physical conditions. They have also been the subject to significant processing and evolution as those physical conditions change, hence we do not expect good agreement with the models. However, this comparison highlights how different the ice inventories are for molecular clouds when compared to these sources. This can give clues as to how different species are being preserved, destroyed or converted into other species as the cloud evolves and collapses to form proto-stellar objects.

In model M1, we observe CO ice is almost at par with H_2O, which is expected in certain scenarios in dense clouds. This is in agreement with RWH16, for which CO ice was produced at par with H_2O ice when competition between diffusive reaction, desorption and accretion was taken into account. In fact, in M2, the abundance of CO ice far exceeds H_2O. In our case, as a result of assuming the diffusion barrier thickness as 2.5 Å (Wakelam et al. 2024), the reaction path of OH + CO $\longrightarrow$ CO_2 + H is more efficient by two orders than the reaction O + HCO $\longrightarrow$ CO_2 + H in agreement with Garrod & Pauly (2011). However, this is still not enough to drive the conversion of CO ice to CO_2 as accretion of CO is two orders of magnitude faster than accretion of CO_2 at this time. Note that for all of the ice species in model M1, the fastest rate is almost always for the movement of molecules from the ice surface to the mantle and vice versa. The over-prediction of CH_4 ice is also a matter of interest. H + CH_3 $\longrightarrow$ CH_4 emerges as the most important reaction forming CH_4 ice on the grain surface which is also the major route of formation as described in the experimental work of Qasim et al. (2020). In contrast, model M2 does not exhibit this over-prediction of ice. Upon further inspection, this can be attributed to inefficient movement of the ices from mantle to the surface at late times in the HH93 model. The disparity between the abundance of H_2CO and other ices in Table 2 between models M1 and M2 can be explained likewise.

The differences in abundances detected in the sources in Table 2 suggest that at the best-fitting time, this model had not attained the expected ratios for most ices with respect to H_2O ice. Further, note that these ratios only give half of the picture. The abundances relative to n_{H}, can also be derived from the corresponding column densities, as in Boogert et al. (2015). Our model predicts these abundances for TMC-1 within one order of magnitude of those observed, suggesting that over the course of the evolution from clouds to proto-stellar objects, the changes occur mostly in the ratios in which these species exist as ices.

4.4. Effects of non-diffusive chemistry

Non-diffusive chemistry facilitates the formation of COMs. As evident from Figure 3, it does not necessarily increase the amount of ices, rather, it assists in the formation of COMs from precursors like methanol. Ices like CH_4, CH_3OH, HCOOH and $HCOOCH_3$ are boosted for both models M3 and M4 (Figure 3). In fact, we see that the number of total ice layers decreases in the case of the HH93 three-phase chemistry prescription and increases in the case of RWH16. For M3, water ice sees a rapid build-up shortly after 1 Myr of evolution, something which is absent in model M4. Specifically, the non-diffusive photodissociation-induced reactions in M3 are more efficient in producing water ice than in M4 in the grain mantle. The formation of water ice can be attributed to the following reactions

$$\text{b-H}_2 + \text{b-OH} \longrightarrow \text{b-H}_2\text{O} + \text{b-H} \qquad \text{(R1)}$$

$$\text{b-CH}_4 + \text{b-OH} \longrightarrow \text{b-CH}_3 + \text{b-H}_2\text{O} \qquad \text{(R2)}$$

The prefix ‘b-’ denotes a species present in the bulk (mantle). Reaction R1 follows a diffusive pathway, as b-H_2 is light enough to

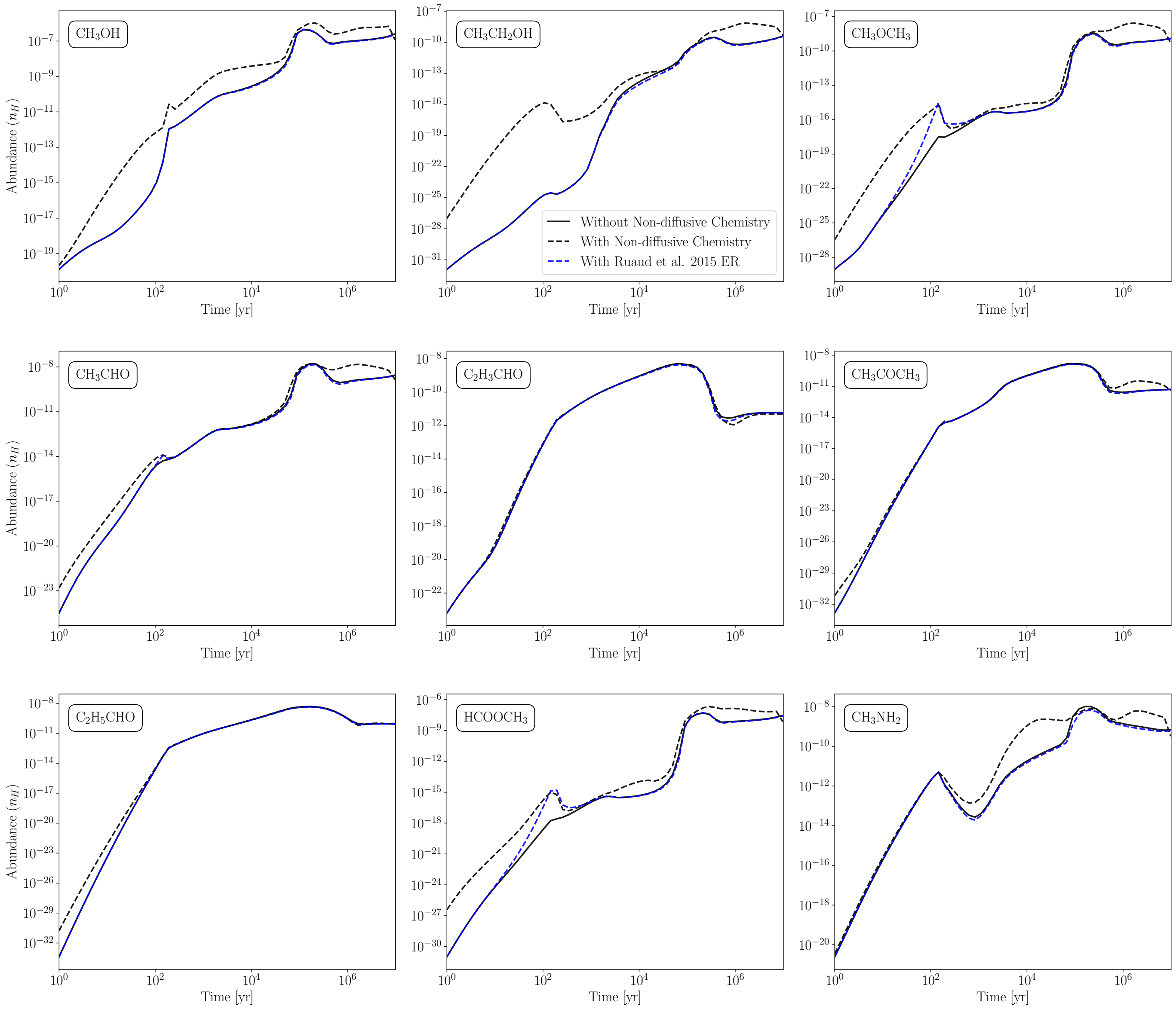

Fig. 7. Abundances of major COMs in gas-phase as a function of time with (model M3) and without (model M1) the inclusion of non-diffusive chemistry.

diffuse readily in cold environments (approximately ∼ 10 K). In contrast, Reaction R2 primarily proceeds via non-diffusive pathways. Both of these reactions exhibit significantly lower rates in model M4. The lack of enough methane ice in the HH93 models is one of the major reasons for which we observe this as Reaction R2 is not as efficient. Further, the inclusion of non-diffusive chemistry boosts abundance of CO$_2$ ice for both the models M3 and M4 as its production no longer relies on the very slowly diffusing CO and O at such low temperature of 10 K. Non-diffusive chemistry enables formation of CO$_2$ without the requirement of diffusion, in agreement with the findings of Jiménez-Serra et al. (2025) where models with non-diffusive chemistry could produce of CO$_2$ ice even at low temperatures of $T_{\rm dust} < 12$ K.

Figure 4 shows that non-diffusive chemistry also does not affect the split between surface and mantle abundances given a three-phase prescription. Enabling non-diffusive chemistry not only makes significant differences in the abundances of major ice species across all models (see Table 2), it also boosts the abundances of COMs in each of them. Non-diffusive chemistry in the case of HH93, could lead to a best-time closer to previous estimates of few Myr. This may be attributed to the fact that non-diffusive chemistry provides extra pathways forming COMs, which are heavier and are susceptible to getting trapped in the mantle, nullify the lesser available concentrations of surface species in the case of HH93. Noting that the effects and trends of non-diffusive chemistry are similar across all models, we limit our discussion and results to the RWH16 models for brevity.

4.4.1. On COMs in the gas-phase

Figure 7 shows abundances of various COMs in gas-phase that have been detected in TMC-1 and are included in the 2024 KIDA network. This evolution of abundances can be thought to occur over three epochs: early stage (from beginning till 10^2 yr), the middle stage (from 10^2 yr to 10^4 yr) and finally the late stage (beyond 10^4 yr). Owing to three distinct phases of evolution, we note there are non-trivial effects on abundances of methanol (CH_3OH), ethanol (CH_3CH_2OH), dimethyl ether (CH_3OCH_3) and methyl formate ($HCOOCH_3$) in the early stage, with rest of species having close to marginal differences between the models with and without non-diffusive chemistry. In the middle stage, ethanol exhibits the greatest deviation from the diffusive-only chemistry once non-diffusive mechanisms are included. In the late stage, which also contains the best-fitting time, the differences for all species gradually decrease as all abundances converge to steady-state. We note that for species like propenal (C_2H_3CHO), acetone (CH_3COCH_3) and propanal (C_2H_5CHO), the negligible differences throughout all stages can be attributed to the fact that these species have a very limited chemical reactions in the 2024 KIDA network with no grain surface reaction (either diffusive or non-diffusive) for propenal, just one pathway for acetone and a couple for propanal.

In our model, most of the gas-phase COMs are majorly produced on the grain surface and subsequently desorbed to gas-phase through the chemical desorption following the prescription from Riedel et al. (2023). Among the pathways only involving gas-phase species, dissociative recombination emerges as sole reaction mechanism. The destruction of gas-phase COMs is also mainly driven by a single mechanism of proton-transfer, where ions like H_3^+ and H_3O^+ act as primary proton donors.

Diffusive chemistry dominates over non-diffusive mechanisms for the gas-phase COMs for which the major formation pathway is successive hydrogenation on the grain-surface followed by reactive desorption in the final step, as the lone H atom is light enough to efficiently diffuse at low temperatures of ~ 10 K. For instance, CH_3OH is most efficiently produced via a diffusive pathway through the hydrogenation of both the methoxy (CH_3O) and hydroxymethyl (CH_2OH) radicals, each contributing approximately 44% to the overall formation. However, in the case of heavier COMs like ethanol (CH_3CH_2OH), for which the major pathway (~ 55%) is

$$\text{s-}CH_3 + \text{s-}CH_2OH \longrightarrow \text{s-}CH_3CH_2OH \longrightarrow CH_3CH_2OH \quad \text{(R3)}$$

where both the reactants are heavy molecules, the non-diffusive pathway dominates. The prefix ‘s-’ denotes the species is an ice and occurs on the grain surface. This trend can be seen for all COMs shown in Figure 7. However, the relative contribution of each chemical process—gas-phase, grain-surface (either diffusive or non-diffusive)—is also time-dependent. For instance, acetaldehyde (CH_3CHO) forms primarily (~53%) through a non-diffusive grain-surface reaction between s-CH_3 and s-HCO at the best-fitting time of 4 Myr. The formation of acetone (CH_3COCH_3), methyl formate ($HCOOCH_3$), and methylamine (CH_3NH_2) is notably dominated by gas-phase processes. Specifically, these molecules are primarily produced via dissociative recombination of their respective protonated precursors—$C_3H_6OH^+$ for acetone (~ 54%), $H_5C_2O_2^+$ for methyl formate (~ 80%), and $CH_3NH_3^+$ for methylamine (~ 69%) at the best-fitting time of 4 Myr. Finally, propanal (C_2H_5CHO) is first formed on the grain surface through a non-diffusive reaction and subsequently desorbs into the gas phase via chemical desorption. Instead of being formed through hydrogenation, its formation occurs via the addition of atomic oxygen to propene (CH_3CHCH_2).

4.4.2. On COMs in the ice-phase

We concentrate our discussion on a subset of the COMs listed in Table 2 as they have been detected in MYSOs, LYSOs and cometary bodies, and on a few oxygen-bearing COMs that have been detected in pre-stellar cores such as L1689B, L1544 and B1-b (Bacmann et al. 2012; Cernicharo et al. 2012; Vastel et al. 2014). The evolution of the fractional abundances with respect to water ice for these are included through Figure 8.

To form methanol (s-CH_3OH) on the grain surface, without non-diffusive chemistry there are two main pathways:

$$\text{s-H} + \text{s-}CH_3O \longrightarrow \text{s-}CH_3OH \quad \text{(R4)}$$

$$\text{s-H} + \text{s-}CH_2OH \longrightarrow \text{s-}CH_3OH \quad \text{(R5)}$$

Reaction R4 represents the final step to form methanol via successive hydrogenation of s-CO, whereas reaction R5 is hydrogenation of the hydroxymethyl radical, which itself originates through H-abstraction of methanol. With non-diffusive chemistry, the reaction s-OH + s-CH_3 $\longrightarrow$ s-CH_3OH also becomes significant through the three-body non-diffusive reaction, but its contribution is still below 1%. This is similar to the findings of Jiménez-Serra et al. (2025), where this pathway was found to produce methanol only marginally, even by the models with non-diffusive chemistry. Overall, the Eley-Rideal non-diffusive reactions dominate all other non-diffusive pathways for methanol. The destruction of s-CH_3OH is also greatly influenced by the inclusion of non-diffusive chemistry. In the diffusive only scenario, methanol is destroyed by reacting with atomic hydrogen leading to the formation of the hydroxy-methyl group (s-CH_2OH) or methoxide (s-CH_3O). Both of these processes are enhanced by three-body and Eley-Rideal non-diffusive mechanisms. Notably, non-diffusive chemistry is more efficient in destroying methanol on grain surfaces than photoprocesses.

For formic acid (s-HCOOH), non-diffusive chemistry greatly boosts the main pathway s-H + s-HOCO $\longrightarrow$ s-HCOOH, with s-OH + s-HCO $\longrightarrow$ s-HCOOH also making a substantial contribution. The latter reaction proceeds through all non-diffusive mechanisms (Eley-Rideal, three-body and photodissociation-induced non-diffusive mechanisms) included in our model and is much more efficient than the diffusive counterpart. Turning on non-diffusive chemistry also enhances the rates of diffusive reactions, as more ices are available to react on the grain surfaces. For acetaldehyde (s-CH_3CHO), we have following pathways

$$\text{s-}CH_3 + \text{s-HCO} \longrightarrow \text{s-}CH_3CHO \quad \text{(R6)}$$

$$\text{s-H} + \text{s-}CH_3CO \longrightarrow \text{s-}CH_3CHO \quad \text{(R7)}$$

We note that R6 is more efficient through the non-diffusive channel and R7 dominates for diffusive chemistry. The inclusion of non-diffusive chemistry also enhances destruction pathways for acetaldehyde, supplementing the conventional photoprocesses and diffusive reactions. We note that all non-diffusive mechanisms are more efficient than photoprocesses but less so than the diffusive counterparts.

The case of dimethyl ether (CH_3OCH_3) is more interesting as it is produced through the following three-body excited non-diffusive reaction (represented as two successive two-body reactions)

$$\text{s-}CH_3^{\star} + \text{s-}H_2CO \longrightarrow \text{s-}CH_3OCH_2, \quad \text{(R8)}$$

$$\text{s-H} + \text{s-}CH_3OCH_2 \longrightarrow \text{s-}CH_3OCH_3 \quad \text{(R9)}$$

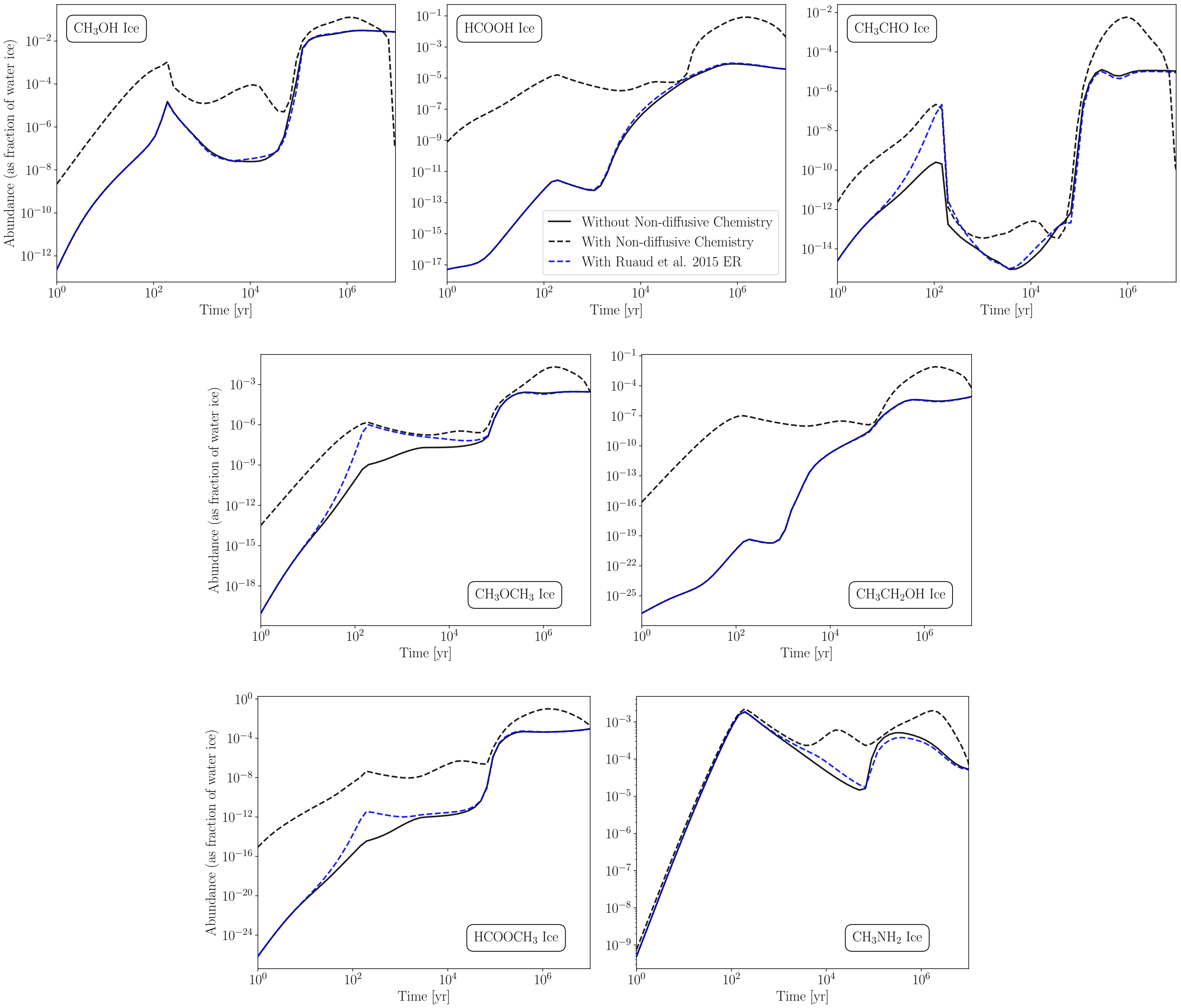

Fig. 8. Abundances of major COM ices as a function of time with (model M3) and without (model M1) the inclusion of non-diffusive chemistry.

Reaction R9 through this mechanism proceeds at a much higher rate than the diffusive counter-part due to the involvemnt of excited s-$CH_3^\star$ ice in R8. The reaction s-CH_3 + s-CH_3O $\longrightarrow$ s-CH_3OCH_3 is the other major pathway to form dimethyl ether on the grain surface. Production of ethanol (s-CH_3CH_2OH) is almost negligible without non-diffusive chemistry, but is amplified by the reaction of a more readily available hydroxy-methyl (s-CH_2OH) reacting with s-CH_3 ice. Notably, turning on non-diffusive chemistry affects the diffusive reaction negatively in this case. Similarly, production of s-$HCOOCH_3$ through the reaction of methoxide (s-CH_3O) with s-HCO becomes much more feasible with non-diffusive chemistry, while suppressing the diffusive pathway. While non-diffusive chemistry produces the smallest difference in abundances for methylamine (s-CH_3NH_2), a new pathway in the form of s-NH_2 + s-CH_3 $\longrightarrow$ s-CH_3NH_2 emerges as one of the major ways to form this nitrogen-bearing COM.

We made the same analysis with model M1 with ER chemistry from Ruaud et al. (2015) activated, and found this was not as efficient as non-diffusive chemistry in producing the COMs discussed here (Figure 8).

5. Conclusions

In this work, we presented a new and flexible astrochemical code which offers a large number of choices and options for exploring the effects of different chemical processes in varying physical conditions for interstellar medium. The key findings are summarized as below.

1. Our benchmarking with well-established models, such as Nautilus, reveals excellent agreement between the two while also highlighting the key differences between the latest 2024 KIDA network and the previously released 2014 version. It also establishes the significance of reproducing identical results from identical initial conditions, implying robustness and stability of the numerical methods used in Pegasis.
2. The importance of grain surface chemistry in cold cores suggests that the three-phase prescription of RWH16 should be

able to capture the surface processes slightly better when compared to HH93 due to greater concentrations of species on the surface.

3. We find that current networks are still lacking in terms of unambiguously reproducing the gas-phase observations of TMC-1 (CP). This can be attributed to a multitude of factors discussed in Wakelam et al. (2024) regarding the uncertainties in the chemical network. We still choose the late time as the best-fitting time on the grounds that it provides the higher mean confidence.
4. The significance of desorption cannot be understated when producing an estimate in chemical ages. Previous works like Garrod et al. (2006) have emphasized on their importance and the process is sensitive to the reaction network, as well as the kinds of desorptive processes considered.
5. The comparison with the ice abundances observed toward BG stars, MYSOs, LYSOs, and cometary bodies provides insights into how much the chemical inventory transforms as the cloud collapses to reach the more evolved protostellar stages.
6. We explore the effects of all non-diffusive mechanisms included in our model on the abundances of COMs. We note that the major reactions are greatly enhanced after enabling non-diffusive chemistry, thereby increasing the share of COMs in both surface and bulk ice.
7. For gas-phase COMs, non-diffusive mechanisms emerge as the dominant pathways for their formation on grain surfaces, followed by chemical desorption, especially when the involved reactants are heavier than atomic hydrogen that do not diffuse efficiently at the low temperatures typical of cold cores.
8. Non-diffusive chemistry also affects the diffusive chemistry, either negatively and positively for different molecules. The Eley-Rideal non-diffusive mechanism and three-body non-diffusive reactions are consistently more efficient than photodissociation-induced non-diffusive reactions, all of which have higher rates than their diffusive counterparts across the COMs.
9. The more general treatment of Eley-Rideal chemistry through non-diffusive means as opposed to the carbon-specific treatment of the Eley-Rideal process in Ruaud et al. (2015) leads to a better estimation of COM abundances in cold cores.
10. The inclusion of non-diffusive chemistry alongside chemisorption makes PEGASIS an extremely versatile astrochemical code, enabling simulations of diverse astrochemical environments with varying grain-surface chemistry and processes. These environments may correspond to cold cores (as in this work) or high-temperature regions (> 100 K), which we will explore in a future study.

Acknowledgements. L.M. expresses his sincere thanks to Valentine Wakelam for permitting the use of the NAUTILUS gas-grain three-phase chemical code in the past, for allowing a detailed benchmark comparison with PEGASIS in this work, and for encouraging the independent development of this new, fast, Python-based astrochemical code within his group. L.M. also thanks Ewine F. van Dishoeck for valuable discussions in the past related to the role of non-diffusive chemistry. L.M. acknowledges financial support from DAE and the DST-SERB research grant (MTR/2021/000864) from the Government of India for this work. This research was carried out in part at the Jet Propulsion Laboratory, which is operated for NASA by the California Institute of Technology. K.W. acknowledges the financial support from the NASA Emerging Worlds grant 18-EW-182-0083. We would like to thank the anonymous referee for constructive comments that helped improve the manuscript.

References

Acharyya, K., Schulte, S. W., & Herbst, E. 2020, ApJS, 247, 4
Agúndez, M., Bermúdez, C., Cabezas, C., et al. 2024, A&A, 688, L31
Agúndez, M., Loison, J.-C., Hickson, K., et al. 2023, A&A, 673, A34
Agúndez, M., Marcelino, N., Tercero, B., et al. 2021, A&A, 649, L4
Agúndez, M., Molpeceres, G., Cabezas, C., et al. 2025, A&A, 693, L20
Agúndez, M. & Wakelam, V. 2013, Chem. Rev., 113, 8710
Andersson, S. & van Dishoeck, E. 2008, A&A, 491, 907
Bacmann, A., Taquet, V., Faure, A., Kahane, C., & Ceccarelli, C. 2012, A&A, 541, L12
Balucani, N., Ceccarelli, C., & Taquet, V. 2015, MNRAS, 449, L16
Bates, D. R. & Spitzer, Jr., L. 1951, ApJ, 113, 441
Bergner, J. B., Öberg, K. I., Garrod, R. T., & Graninger, D. M. 2017a, ApJ, 841, 120
Bergner, J. B., Öberg, K. I., & Rajappan, M. 2017b, ApJ, 845, 29
Boogert, A. C. A., Gerakines, P. A., & Whittet, D. C. B. 2015, ARA&A, 53, 541
Cabezas, C., Agúndez, M., Marcelino, N., et al. 2025, A&A, 693, L14
Cazaux, S. & Tielens, A. 2002, ApJ, 575, L29
Cernicharo, J., Cabezas, C., Agúndez, M., et al. 2024a, A&A, 688, L13
Cernicharo, J., Cabezas, C., Fuentetaja, R., et al. 2024b, A&A, 690, L13
Cernicharo, J. & Guelin, M. 1987, A&A, 176, 299
Cernicharo, J., Marcelino, N., Roueff, E., et al. 2012, ApJ, 759, L43
Chang, Q. & Herbst, E. 2016, ApJ, 819, 145
Collings, M. P., Anderson, M. A., Chen, R., et al. 2004, MNRAS, 354, 1133
Cuppen, H., Karssemeijer, L., & Lamberts, T. 2013, Chem. Rev., 113, 8840
Das, A., Majumdar, L., Sahu, D., et al. 2015, ApJ, 808, 21
Draine, B. T. & Sutin, B. 1987, ApJ, 320, 803
Du, F. 2021, Res. Astron. Astrophys., 21, 077
Fayolle, E. C., Öberg, K., Cuppen, H. M., Visser, R., & Linnartz, H. 2011, A&A, 529, A74
Fuente, A., Navarro, D., Caselli, P., et al. 2019, A&A, 624, A105
Fuentetaja, R., Agúndez, M., Cabezas, C., et al. 2024, A&A, 688, L15
Furuya, K., Aikawa, Y., Hincelin, U., et al. 2015, A&A, 584, A124
Furuya, K., Drozdovskaya, M., Visser, R., et al. 2017, A&A, 599, A40
Garrod, R. 2008, A&A, 491, 239
Garrod, R., Park, I. H., Caselli, P., & Herbst, E. 2006, Faraday Discuss., 133, 51
Garrod, R. T. 2013, ApJ, 765, 60
Garrod, R. T. & Herbst, E. 2006, A&A, 457, 927–936
Garrod, R. T. & Pauly, T. 2011, ApJ, 735, 15
Garrod, R. T., Wakelam, V., & Herbst, E. 2007, A&A, 467, 1103
Geppert, W. D. & Larsson, M. 2008, Mol. Phys., 106, 2199
Gould, R. J. & Salpeter, E. E. 1963, ApJ, 138, 393
Govers, T. R., Mattera, L., & Scoles, G. 1980, J. Chem. Phys., 72, 5446
Gratier, P., Majumdar, L., Ohishi, M., et al. 2016, ApJS, 225, 25
Gredel, R. 1990, in Molecular Astrophysics, ed. T. W. Hartquist, 305
Gredel, R., Lepp, S., & Dalgarno, A. 1987, ApJ, 323, L137
Gredel, R., Lepp, S., Dalgarno, A., & Herbst, E. 1989, ApJ, 347, 289
Hartmann, L., Ballesteros-Paredes, J., & Bergin, E. A. 2001, ApJ, 562, 852
Hartquist, T., Williams, D., & Viti, S. 2001, A&A, 369, 605
Hasegawa, T. I. & Herbst, E. 1993a, MNRAS, 261, 83
Hasegawa, T. I. & Herbst, E. 1993b, MNRAS, 263, 589
Hasegawa, T. I., Herbst, E., & Leukng, C. M. 1992, ApJS, 82, 167
Herbst, E. 1995, Annu. Rev. Phys. Chem., 46, 27
Herbst, E. 2001, Chem. Soc. Rev., 30, 168–176
Herbst, E., Chang, Q., & Cuppen, H. M. 2005, in Journal of Physics Conference Series, Vol. 6, Journal of Physics Conference Series (IOP), 18–35
Herbst, E. & Klemperer, W. 1973, ApJ, 185, 505
Herbst, E. & van Dishoeck, E. F. 2009, ARA&A, 47, 427
Hindmarsh, A. C. 1983, in IMACS Transactions on Scientific Computation, Vol. 1, Scientific Computing, ed. R. S. S. et al. (Amsterdam: North-Holland), 55–64
Holbrook, K. A., Pilling, M. J., & Robertson, S. H. 1996, Unimolecular reactions, 2nd edn. (Wiley)
Holdship, J., Viti, S., Jiménez-Serra, I., Makrymallis, A., & Priestley, F. 2017, AJ, 154, 38
Jiménez-Serra, I., Megías, A., Salaris, J., et al. 2025, A&A, 695, A247
Jin, M. & Garrod, R. T. 2020, ApJS, 249, 26
Kaifu, N., Ohishi, M., Kawaguchi, K., et al. 2004, Publ. Astron. Soc. Jpn., 56, 69
Kalvāns, J. & Shmeld, I. 2010, A&A, 521, A37
Kalvāns, J. 2014, A&A, 573, A38
Katz, N., Furman, I., Biham, O., Pirronello, V., & Vidali, G. 1999, ApJ, 522, 305
Kooij, D. M. 1893, ZPhCh, 12U, 155–161
Lam, S. K., stuartarchibald, Pitrou, A., et al. 2024, numba/numba: 0.60.0
Le Teuff, Y. H., Millar, T. J., & Markwick, A. J. 2000, A&AS, 146, 157
Lee, H. H., Herbst, E., Pineau des Forets, G., Roueff, E., & Le Bourlot, J. 1996, A&A, 311, 690
Li, X., Heays, A. N., Visser, R., et al. 2013, A&A, 555, A14
Loison, J.-C., Wakelam, V., Hickson, K. M., Bergeat, A., & Mereau, R. 2013, MNRAS, 437, 930

Majumdar, L., Gratier, P., Ruaud, M., et al. 2017, MNRAS, 466, 4470
Maret, S., Bergin, E., & Tafalla, M. 2013, A&A, 559, A53
McElroy, D., Walsh, C., Markwick, A., et al. 2013, A&A, 550, A36
McGuire, B. A. 2022, ApJS, 259, 30
Millar, T., Walsh, C., Van de Sande, M., & Markwick, A. 2024, A&A, 682, A109
Millar, T. J., Bennett, A., Rawlings, J. M. C., Brown, P. D., & Charnley, S. B. 1991, A&AS, 87, 585
Millar, T. J., Farquhar, P. R. A., & Willacy, K. 1997, A&AS, 121, 139
Minissale, M., Dulieu, F., Cazaux, S., & Hocuk, S. 2016, A&A, 585, A24
Mouschovias, T. C., Tassis, K., & Kunz, M. W. 2006, ApJ, 646, 1043
Mumma, M. J. & Charnley, S. B. 2011, ARA&A, 49, 471
Navarro-Almaida, D., Fuente, A., Majumdar, L., et al. 2021, A&A, 653, A15
Öberg, K. I., Fuchs, G. W., Awad, Z., et al. 2007, ApJ, 662, L23
Öberg, K. I., Garrod, R. T., van Dishoeck, E. F., & Linnartz, H. 2009, A&A, 504, 891
Prasad, S. S. & Tarafdar, S. P. 1983, ApJ, 267, 603
Qasim, D., Fedoseev, G., Chuang, K. J., et al. 2020, Nat. Astron, 4, 781
Rachid, M., van Scheltinga, J. T., Koletzki, D., & Linnartz, H. 2020, A&A, 639, A4
Reboussin, L., Wakelam, V., Guilloteau, S., & Hersant, F. 2014, MNRAS, 440, 3557–3567
Remijan, A. J., Changala, P. B., Xue, C., et al. 2025, ApJ, 982, 191
Riedel, W., Sipilä, O., Redaelli, E., et al. 2023, A&A, 680, A87
Roberge, W. G., Jones, D., Lepp, S., & Dalgarno, A. 1991, ApJS, 77, 287
Rocha, W., van Dishoeck, E., Ressler, M., et al. 2024, A&A, 683, A124
Ruaud, M., Loison, J., Hickson, K., et al. 2015, MNRAS, 447, 4004
Ruaud, M., Wakelam, V., & Hersant, F. 2016, MNRAS, 459, 3756–3767
Rubin, M., Altwegg, K., Balsiger, H., et al. 2019, MNRAS, 489, 594
Semenov, D., Hersant, F., Wakelam, V., et al. 2010, A&A, 522, A42
Shen, C., Greenberg, J., Schutte, W., & Van Dishoeck, E. 2004, A&A, 415, 203
Shingledecker, C. N., Tennis, J., Le Gal, R., & Herbst, E. 2018, ApJ, 861, 20
Sipilä, O., Caselli, P., Redaelli, E., & Spezzano, S. 2022, A&A, 668, A131
Smith, I. W., Herbst, E., & Chang, Q. 2004, MNRAS, 350, 323
Sternberg, A., Dalgarno, A., & Lepp, S. 1987, ApJ, 320, 676
Taquet, V., Ceccarelli, C., & Kahane, C. 2012, A&A, 538, A42
Terwisscha van Scheltinga, J., Ligterink, N., Boogert, A., Van Dishoeck, E., & Linnartz, H. 2018, A&A, 611
Terwisscha van Scheltinga, J. T., Marcandalli, G., McClure, M. K., Hogerheijde, M. R., & Linnartz, H. 2021, A&A, 651, A95
Tielens, A. G. G. M. & Allamandola, L. J. 1986, Composition, structure, and chemistry of interstellar dust.
Tielens, A. G. G. M. & Hagen, W. 1982, A&A, 114, 245
Umebayashi, T. 1983, Prog. Theor. Phys., 69, 480
Vastel, C., Ceccarelli, C., Lefloch, B., & Bachiller, R. 2014, ApJ, 795, L2
Vasyunin, A. I., Caselli, P., Dulieu, F., & Jiménez-Serra, I. 2017, ApJ, 842, 33
Vasyunin, A. I. & Herbst, E. 2013, ApJ, 769, 34
Vidal, T. H., Loison, J.-C., Jaziri, A. Y., et al. 2017, MNRAS, 469, 435
Vidali, G., Roser, J. E., Ling, L., et al. 2006, Faraday Discuss., 133, 125
Visser, R., Van Dishoeck, E., & Black, J. H. 2009, A&A, 503, 323
Wakelam, V., Dartois, E., Chabot, M., et al. 2021, A&A, 652, A63
Wakelam, V., Gratier, P., Loison, J.-C., et al. 2024, A&A, 689, A63
Wakelam, V., Herbst, E., Loison, J.-C., et al. 2012, ApJS, 199, 21
Wakelam, V., Loison, J.-C., Herbst, E., et al. 2015, ApJS, 217, 20
Wakelam, V., Smith, I. W. M., Herbst, E., et al. 2010, Space Sci. Rev., 156, 13
Watson, W. D. 1973, ApJ, 183, L17
Watson, W. D. 1974, ApJ, 188, 35
Watson, W. D. 1976, Rev. Mod. Phys., 48, 513
Wenzel, G., Cooke, I. R., Changala, P. B., et al. 2024, Science, 386, 810
Willacy, K. & Millar, T. J. 1998, MNRAS, 298, 562
Woodall, J., Agúndez, M., Markwick-Kemper, A., & Millar, T. 2007, A&A, 466, 1197
Woon, D. E. & Herbst, E. 2009, ApJS, 185, 273

Appendix A: Generation of non-diffusive reactions

To generate the reaction set for each non-diffusive mechanism discussed in the work, we start with grain-surface and bulk-ice reactions of the 2024 KIDA network. To generate the set for photodissociation-induced non-diffusive reactions, we identify all the species which are produced through photodissociations by UV photons on grain surfaces and photodissociations by cosmic-ray induced UV photons on grain surfaces. These are the `type 17, 18, 19, 20` in the reaction network (Wakelam et al. 2024). Once we have these photoproducts, we move to `type 14` which represents all diffusive reactions, to identify the subset of reactions where the photoproducts participate as reactants, giving us the required reaction set. In the case of non-diffusive Eley-Rideal reactions, similar process is performed, except this time, we take products from `type 99`, which represents adsorption reactions on grains. In the subset of diffusive reactions where these products occur as reactants, it ensures that one reactant has already accreted on the grain-surface and it immediately encounters the other reactant there. Further, we ensure that the complete reaction is a surface-only process with no bulk-ice species involved, as is the case with E-R. Finally, to generate the non-diffusive three-body reactions, we need to select the subset of diffusive reactions for both grain-surface and grain-mantle where both involved reactants occur as products of diffusive reactions itself. To this end, we take products from `type 14`, and then proceed similar to previous cases to generate the reaction set for this mechansim. The following two grain-surface reactions are added separately for the three-body excited formation mechanism (Jin & Garrod 2020)

$$\text{s-CH}_3^\star + \text{s-CO} \longrightarrow \text{s-CH}_3\text{CO} \tag{AR1}$$

$$\text{s-H} + \text{s-CH}_3\text{CO} \longrightarrow \text{s-CH}_3\text{CHO} \tag{AR2}$$

and

$$\text{s-CH}_3^\star + \text{s-H}_2\text{CO} \longrightarrow \text{s-CH}_3\text{OCH}_2 \tag{AR3}$$

$$\text{s-H} + \text{s-CH}_3\text{OCH}_2 \longrightarrow \text{s-CH}_3\text{OCH}_3 \tag{AR4}$$

under the constraint that s-$CH_3^\star$ ice is formed by the following reaction

$$\text{s-H} + \text{s-CH}_2 \longrightarrow \text{s-CH}_3^\star \tag{AR5}$$

Jin & Garrod (2020) discuss an additional reaction that undergoes a non-diffusive process via the formation of an excited intermediate. However, this reaction was not included because one of its participants (s-CH_3OCO) is not present in the 2024 KIDA network.

Appendix B: Benchmarking Pegasis

We depict time evolution of select species detected in TMC-1 (CP) using the both 2014 and 2024 KIDA networks with Pegasis and Nautilus. The oxygen-bearing species are shown in Figure B.1, with hydrocarbons in Figure B.2, nitrogen-bearing in Figures B.3, B.4 and sulfur-bearing species follow in Figure B.5. For visual clarity, the Nautilus results were over-plotted over Pegasis results through orange-colored markers. As is evident from the figures, Pegasis and Nautilus have excellent agreement, with the plots of both models exhibiting high co-incidence.

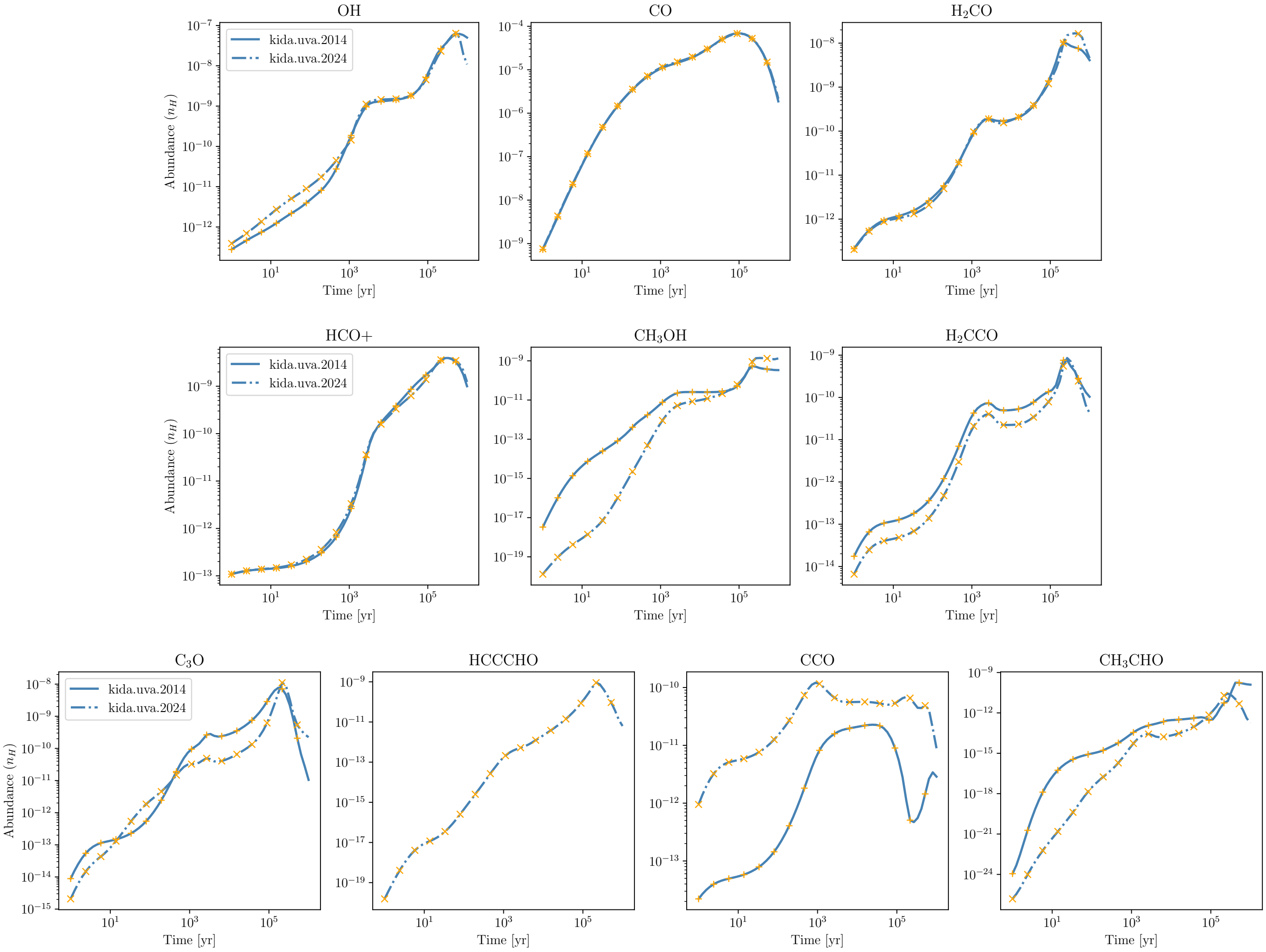

Fig. B.1. Comparison of selected oxygen-bearing species in gas-phase detected in TMC-1 molecular cloud. Both Pegasis (blue lines) and Nautilus (orange markers) have excellent agreement for both the networks (2014 is represented by dash-dotted lines and 2024 represented by solid lines).

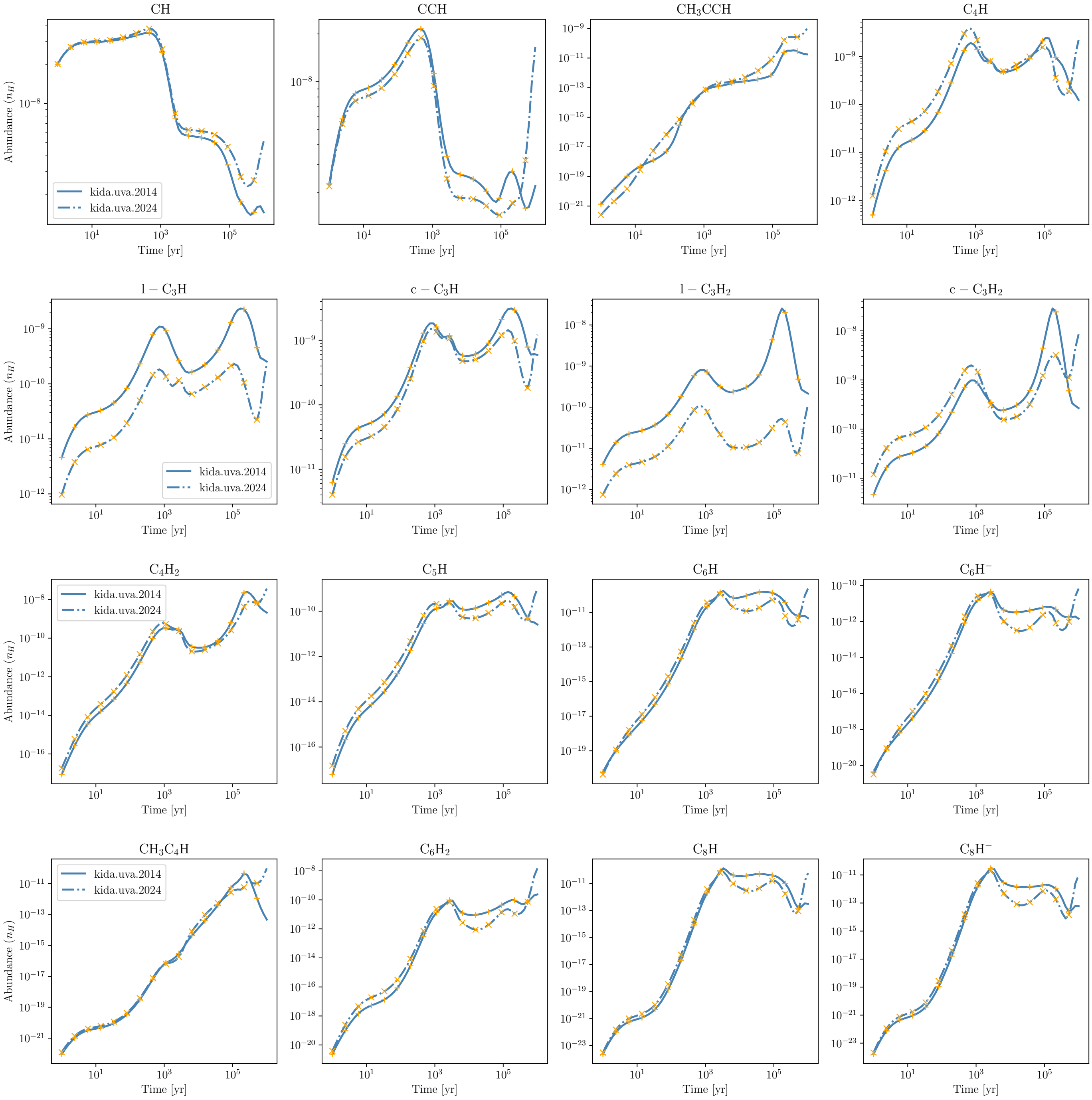

Fig. B.2. Same as Figure B.1, but for hydrocarbons.

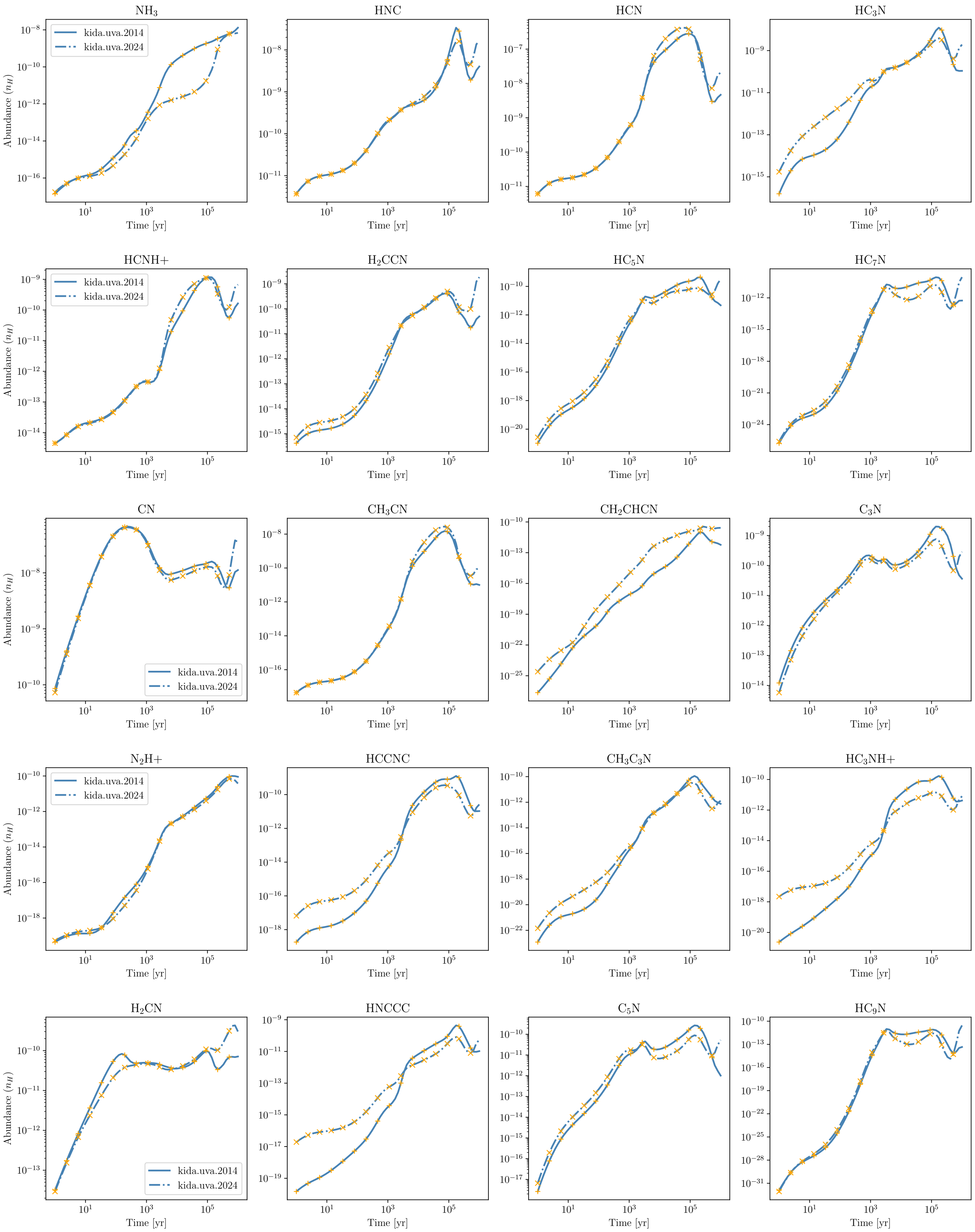

Fig. B.3. Same as Figure B.1, but for nitrogen-bearing species.

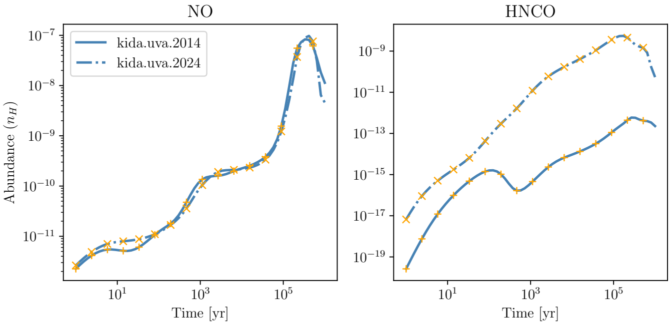

Fig. B.4. Same as Figure B.1, but for NO-bearing species.

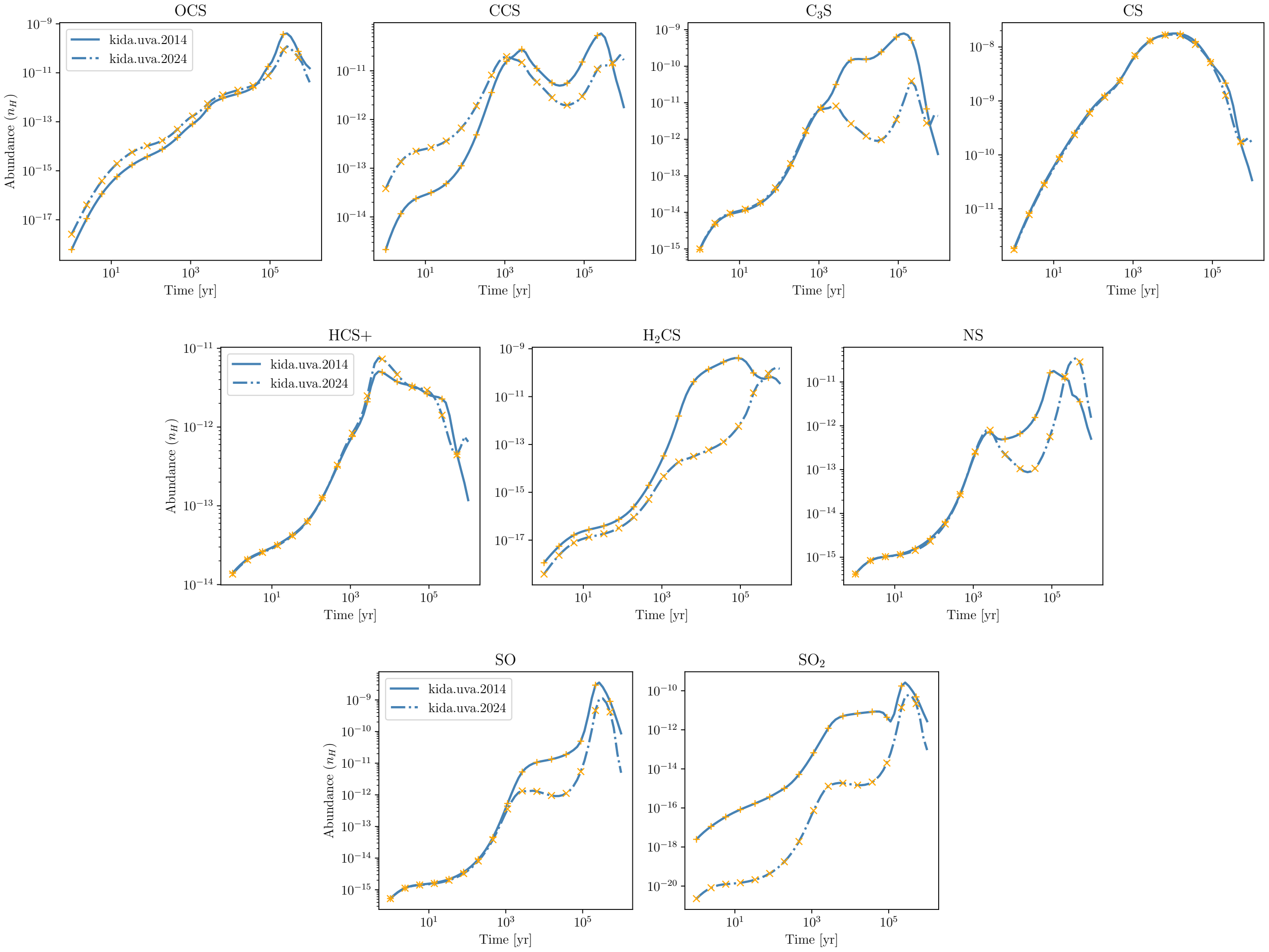

Fig. B.5. Same as Figure B.1, but for sulfur-bearing species.